Pontine pathology mediates common symptoms of blast-induced chronic mild traumatic brain injury

James S. Meabon[1,2]*, Abigail G. Schindler[2,3], Daniel R. Murray[1], Elizabeth A. Colasurdo[1], Carl L. Sikkema[1], Joshua W. Rodriguez[1], Mohamed Omer[1], Marcella M. Cline[4], Aric F. Logsdon[3], Donna J. Cross[5], Todd L. Richards[6], Kole D. Meeker[3,7], Andrew Shutes-David[1,3], Mayumi Yagi[3], Daniel P. Perl[8], Desiree A. Marshall[9], C. Dirk Keene[9], William A. Banks[2,3,11], Ronald G. Thomas[12,13], Cory McEvoy[14], Adam Crabtree[14], Jake R. Powell[15], Jason P. Mihalik[15], Kathleen F. Pagulayan[1,16], Murray A. Raskind[1,2], Elaine R. Peskind[1,2], & David G. Cook[3,10,11]

[1] VA Northwest Mental Illness Research, Education, and Clinical Center (MIRECC), VA Puget Sound Health Care System (VA Puget Sound), Seattle, WA, USA.

[2] Department of Psychiatry and Behavioral Sciences, University of Washington, Seattle, WA, USA.

[3] Geriatric Research, Education, and Clinical Center (GRECC), VA Puget Sound Health Care System (VA Puget Sound), Seattle, WA, USA.

[4] Department of Molecular and Cellular Biology, University of Washington, Seattle, WA, USA.

[5] Department of Radiology, University of Utah, Salt Lake City, UT, USA.

[6] Department of Radiology, University of Washington, Seattle, WA, USA.

[7] Immusoft, Seattle, WA, USA.

[8] Department of Pathology, DoD/USU Brain Tissue Repository and Neuropathology Core Laboratory, Uniformed Services University, Bethesda, MD, USA.

[9] Department of Laboratory Medicine and Pathology, University of Washington, Seattle, WA, USA.

[10] Department of Pharmacology, University of Washington, Seattle, WA, USA.

[11] Department of Medicine, University of Washington, Seattle, WA, USA.

[12] Alzheimer's Disease Cooperative Study, University of California San Diego, La Jolla, CA, USA.

[13] Division of Biostatistics, Department of Family Medicine & Public Health, University of California San Diego, La Jolla, CA, USA.

[14] United States Army Special Operations Command, Fort Bragg, NC, USA.

[15] Physical Therapy, Department of Allied Health Sciences, School of Medicine, University of North Carolina, Chapel Hill, NC, USA.

[16] Department of Rehabilitation Medicine, University of Washington, Seattle, WA, USA.

* To whom correspondence should be addressed:

James S. Meabon, PhD

MIRECC, VA Puget Sound Health Care System

Department of Psychiatry and Behavioral Science

University of Washington School of Medicine

1660 S. Columbian Way

Seattle, WA 98108 USA

Phone: 206-277-4631

Email: james64@uw.edu

Abstract

Understanding how diffuse mild traumatic brain injuries can provoke common and persistent post-concussive symptoms (PCS), such as impaired sleep, is crucial to prevent and treat chronic disability and neurodegeneration. We mapped the spatially-resolved single cell landscape of diffuse mTBI pathology in a mouse model of blast exposure; identifying brainstem injuries predictive of later PCS. Repeated mTBI was necessary to establish chronic microglial activation and phagocytosis of myelin in the pontine reticular formation; where IL33 release by oligodendrocytes predicted microgliopathy. In postmortem brainstem tissues from patients with traumatic brain injury, chronic microglial activation and myelin phagocytosis was evident up to 20 years after diffuse mTBI caused by blast. In living patients with chronic blast mTBI, myelin injury in pontine projections mediated sleep disturbance and other PCS, with a dose dependent effect of mTBI number on sleep disturbance severity. These results support a mechanism for diffuse mTBIs to cause delayed persistent PCS.

Main

Mild traumatic brain injuries (mTBIs), or concussions, account for ~55 million annual global TBI cases.[1] Although the causes of these injuries vary, persistent post-concussive symptoms (PCS) following mTBI—e.g., development of impairments in concentration, memory, mood, sensation, and sleep—are remarkably consistent.[2] This consistency suggests that mTBIs share a common underlying neuropathology that may map to specific brain areas subserving these functions (e.g., brainstem nuclei). However, the mechanisms underlying these deficits are poorly understood, in part because mTBIs are undetectable on clinical neuroimaging.

Evidence suggests that TBIs may provoke the delayed development of deficits via neuroimmune axes that regulate the microstructural repair of the nervous system.[3,4] This means that two critical determinants of long-term TBI outcomes are injury location and the subsequent cellular response. An improved anatomical understanding of specific TBI pathologies under conditions of diffuse injury, such as those caused by blast shock waves moving through the brain, could help predict the development of generalized functional or behavioral deficits following disease onset. Recent advances in high-dimensional spatially-resolved phenotyping coupled with precise anatomical brain mapping may help us understand how changes in the pathological microenvironment relate to persistent PCS following mTBI.

Even with minimal rotational head or body displacement, mTBI caused by exposure to explosive overpressures transmits a rapid force throughout the brain, diffusely injuring its tissues. The resulting pathology often differs from more kinetic forms of mTBI (e.g., caused by falls, assaults, etc.);[5] however, blast-mTBIs often cause persistent PCS that are indistinguishable from other mTBIs.[6-11] Therefore, we examined mTBIs associated with blast overpressure exposure in both military veterans and a mouse model of blast-mTBI with attenuated head

103 movement.[12] This approach avoids coup-contrecoup and "whiplash" injuries, while testing the
104 hypothesis that blast-mTBIs provoke conserved post-concussive symptoms mediated by chronic
105 pathological changes in brainstem nuclei.

106 **Results**

107 **Brainstem nuclei are vulnerable to mTBI**

108 Post-concussive symptoms typically relate to microscopic traumatic axonal injuries near small
109 blood vessels[13,14] in specific anatomical regions, such as cerebellum and corpus callosum,[13]
110 where vessel lesions can drive circuit dysfunction.[15] Functional injury of microvascular tight
111 junctions can be assessed by measuring the leakage of blood-borne molecules into the brain
112 parenchyma. This method paradoxically shows that after TBI, disruption of the blood-brain
113 barrier to the large molecule human albumin (66 kDa) is detectable prior to disruption to the
114 smaller molecule sucrose (342 Da). However, disruption to sucrose persists longer than
115 disruption to human albumin.[16] We measured the functional integrity of the blood-brain barrier
116 across brain regions 15 minutes to 3 days after a single blast-mTBI using blood-borne ^{14}C-
117 sucrose and ^{99m}Tc-Albumin. Although a non-significant accumulation of sucrose and albumin
118 was observed in the cortex during the acute phase (15 min after mTBI), significant leakages of
119 both large and small molecules were detected in the brainstem, but not cortex (**Fig. 1a**). This
120 indicates a regional vulnerability of the blood-brain barrier (BBB) to injury, with the brainstem's
121 BBB being more susceptible to injury after a single mTBI than the cortex. Injured neurons in
122 areas of microvascular disruption can be identified by their uptake of blood-borne dyes that leak
123 into the brain across the disrupted BBB, whereas adjacent uninjured neurons remain unlabeled.[17]
124 We used this method to determine the relative frequency of injured neurons across brain regions

and white versus gray matter (**Fig. 1b, c**). Projection neurons, which are clearly distinguished from glia using this method (**Fig. 1d, e**), were labeled by extravasated fluorescent dye and occurred most frequently in the brainstem. In the brainstem, about 30% of mice showed evidence of neuronal injury within one hour and up to 70% of mice had observable neuronal injury within four hours of a single mTBI (**Fig. 1b**). Across sagittal brainstem sections, labeled cells occurred most frequently in white matter (**Fig. 1c**). Blood-borne labeling of injured brainstem neurons was visually more subtle than injured Purkinje cells of the inferior cerebellum (**Fig 1d**), a classic injury pattern of mTBI,[18] likely owing to their expansive and dense arborizations.

Injured brainstem neurons and areas of BBB damage coincided with local changes in microglial morphology that are consistent with activation and phagocytosis of extravasated materials (**Fig. 1d**). Diffuse axonal and neuronal injuries were primarily observed in the pontine reticular formation (RF), one of several brainstem regions controlling sleep behavior (**Fig. 1e**). Localized cellular injuries were observed laterally toward the brainstem surface, with frequent prominent injuries along the ventral caudal surface, spinal trigeminal tract, and dorsal columns and was independently identified by unguided investigators (AFL, KDM) blinded to the study groups.

The development of brainstem tauopathy, indicating axon injury, paralleled increased expression of aquaporin-4 (AQP4), which regulates the brain-wide convection of water. A compensatory increase in the expression of magnesium superoxide dismutase (MnSOD), a mitochondrial redox enzyme responsive to TBI-related cellular injury,[12] paralleled the increase in the fluorescent labeling of injured neurons (**Fig. 1f**). Tauopathy in the pontine gray, medial lemniscus, and RF persisted at least 24 hours after injury (**Fig. 1g, h**).

Cerebral edema often follows both clinical and experimental mTBI despite unremarkable neuroimaging results. We postulated that the prominence of diffuse injury from the foramen magnum to the 4th ventricle and the related changes in the AQP4 water transporter would be accompanied by tissue swelling. Such swelling, we posited, would result in reduced 4th ventricle volume per T2 MRI and be associated with secondary cerebral edema, yielding enlargement of the 3rd and lateral cerebral ventricles. In group-blinded analyses of mice assessed 24 hours after a single blast-mTBI, we found that mTBI induced significant enlargement of the lateral and 3rd ventricular volume while reducing the 4th ventricular volume (**Fig. 1i, j**). These results indicate that a single blast-mTBI can cause axonal injury and inflammation of the brainstem in the absence of gross hemorrhage. Such injuries may contribute to more expansive secondary injuries related to edema throughout the brain.[19]

mTBI establishes persistent brainstem microgliopathy

Repetitive mTBI is an environmental risk factor for chronic neurodegenerative phenotypes.[20-22] Genetic risk factors for neurodegeneration often map to myeloid cells, including peripheral blood monocytes and brain resident microglia.[23] However, our understanding of how disease-associated immune phenotypes relate to TBI pathologies is incomplete. To determine the relationship between myeloid phenotypes and the neuropathological landscape of the tissue microenvironment after repeated mTBI, we first tested the *a priori* hypothesis that functional alterations in brain myeloid cells would be a persisting and sensitive indicator of regional injury, with the greatest changes occurring in the brainstem as seen during acute injury. To evaluate this hypothesis, we used a RiboTag strategy to assess the active translatome specifically in brain myeloid cells from mice with repeated TBI or sham exposure (1 per day for 3 days), avoiding the trauma-induced changes in gene signatures evoked by *ex vivo* dissection of live tissue and cell

sorting that are known to occur.[24,25] By using a tamoxifen-inducible CX3CR1-creER mouse line shown to be superior in achieving brain macrophage specificity with the exclusion of neuron-derived contaminating mRNA,[24] we employed a discovery approach followed by validation in an additional secondary cohort to identify candidate genes differentially expressed across brainstem, cerebellum, and cortical tissues in mice one month after repetitive mTBI (3x; 1 per day for 3 days), as compared with gene levels in tamoxifen-induced CX3CR1-creER control mice receiving an equal number of sham-TBI treatments (**Fig. 2a, b, c**). Brainstem tissues showed more differentially expressed myeloid genes than cerebellar or cortical tissues consistent with acute injury patterns being concentrated in the brainstem.

We then performed gene ontology (GO) term analysis. Given that significantly fewer genes were confirmed in the cortex and cerebellum, only differentially expressed genes confirmed in brainstem tissue were used (**Fig. 2d**). In agreement with previous reports, blast-mTBI–induced geneset enrichments in brainstem myeloid cells included programs for macromolecular binding (e.g., *APOE*), lytic vacuole (e.g., *CD68*), exosome, cell adhesion and locomotion.[23]

Given that microglial properties shift in response to the conditions of their tissue microenvironments, we developed an imaging mass cytometry (IMC) workflow to visualize how the relations between microglial phenotypes and their tissue microenvironments changed in response to TBI (**Fig. 2e**). To do this, we developed a panel of 35 metal-labeled antibodies specific to murine TBI histology, including cellular, pathological, and signaling markers (**Table S2**). Antibody-stained tissue slides were then laser-ablated and the subsequent signal was detected with time-of-flight mass spectrometry, producing a 2-dimensional, rasterized

representation of metal abundances analogous to a highly-multiplexed microscope image. Following *in silico* image segmentation into single cells in CellProfiler, analyses were conducted in HistoCAT and R. We identified 256,295 cells from images of 8 coronal pontine hemisections that were taken from randomly selected study mice and that provide tissue representation of ventral pontine and dorsal structures near the 4th ventricle (**Fig. 2e)**.

Phenotyping based on nonlinear dimensionality reduction was implemented using Barnes-Hut t-distributed stochastic neighbor embedding (t-SNE) (**Fig. 2f; Fig. S1**). To define the prominent microenvironmental phenotypes of single cells in the injured brain, we used unbiased phenograph-based clustering to yield 36 distinct clusters for further analysis (**Fig. 2g**). This method differentiated both unreactive microglia (cluster 4; Iba^{+}, CCR2^{-}, CD68^{lo}, ApoE^{lo}) and a disease-associated microglial (DAM) phenotype (cluster 26; Iba^{+}, CCR2^{-}, CD63^{+}, CD68^{hi}, ApoE^{hi}) consistent with single-cell RNA sequencing analyses of Alzheimer's disease brain and neurodegenerative models,[23,26,27] in addition to several non-microglial phenotypes representing neuronal, vascular, glial, and peripheral immune cells. Intercellular associations, as measured by neighborhood analysis, increased between spatially resolved disease-associated microglia with IL33^{+} myelin (clusters 6 and 17), NeuN^{+} neurons (cluster 13) and HTT^{+} neurons (cluster 24) in brain-injured mice whereas similar associations did not change in control mice (**Fig. 2h**). Taken together, these findings suggest that repetitive mTBI provokes a persisting pontine microgliopathy that is associated with slowly resolving neuronal and IL33^{+} myelin injury, which can be spatially resolved and quantified using unbiased computational means.

Myelin injury precedes sleep deficits

Delayed-onset PCS are thought to reflect progressive changes in cellular phenotypes prior to functional and structural brain changes. We used a data-driven approach to agnostically identify specific regions of persisting brainstem pathology that could cause persistent PCS. More specifically, we gated on disease-associated microglia in IMC images and measured their average frequency distributions (i.e., DAM/total microglia) per subject across exclusive brain-region image masks of whole pontine hemisections. We then used the results to inform later hypothesis testing on the relations between pathology, chronic symptoms, and the known functions of the brain regions. Representative IMC images of pontine disease-associated microglia in blast-mTBI and sham control mice are shown in **Figure 3a**. TBI increased the frequencies of disease-associated microglia in several areas with post-hoc FDR-adjusted analyses identifying notable increases in the reticular formation (rf; $t[62]=3.366$, $q=0.0019$), spinal trigeminal nerve tract (spn; $t[62]=3.066$, $q=0.0034$), ventral white matter (vwm; $t[62]=3.317$, $q=0.0019$), and ventral cochlear nucleus (vco; $t[62]=6.448$, $q<0.0001$) (**Fig. 3b**). Since blast-mTBI induces the association of DAM with myelin expressing the alarmin molecule IL33 (**Fig. 2i**), we examined the expression of IL33 among all 44,023 spatially resolved single $CNPase^{+}/IL33^{+}$ oligodendrocytes distributed across these regions. Post-mTBI oligodendrocytes of several pontine regions showed significant loss of the alarmin IL33 (vii: $t[42]=1.98$, $q=0.05$; rf: $t[42]=3.225$, $q=0.0062$; in: $t[42]=3.406$, $q=0.0062$; spv: $t[42]=3.108$, $q=0.0062$; spn: $t[42]=2.782$, $q=0.0118$; pyr: $t[42]=2.3$, $q=0.0278$; pcg: $t[42]=2.711$, $q=0.0118$; **Fig. 3c**), through its apparent release from nuclear stores into the surrounding microenvironment (**Fig. 3d**). Microglia, which express IL33R mRNA (**Fig. 3e**), accumulate in a predictive linear manner driven by IL33 levels (**Fig. 3f**).

Next, we used a false-discovery rate-adjusted method to focus our analysis on the pontine structure(s) displaying the most consistently altered IL33 expression following TBI. We found highly significant mean IL33 reductions per oligodendrocyte for each blast and sham mouse in the RF indicating robust and persisting white matter injury (**Fig. 3g**). Disease-associated microglia heavily express the lytic vacuole protein CD68, which is known to facilitate phagocytotic clearance of diseased tissue, including myelin.[17,28] CNPase is an integral myelin protein required for axon paranode maintenance[29] in that its axoglial decoupling is associated with progressive axonal degeneration[30] and phagocytosis by microglia during dysmyelination[29] and Wallerian degeneration.[31] Because IMC is limited to 2D analyses, we used 3D confocal microscopy of sagittal brainstem sections near midline to measure how microglial internalization of CNPase relates to both injury location across brainstem structures and the number of blast-mTBIs administered. Phagocytosis of CNPase by both single-cell and clustered microglia was observed in pons and medulla, with greater apparent co-localization observed in microglial nodules than single microglia (**Fig. 3h, arrowheads**). One month after single or repeated (3x) blast-mTBI, myelin consumption was measured as the number of CNPase-positive voxels inside Iba-1-stained microglial volumes. Myelin consumption by microglia increased in relation to the number of mTBIs ($F(2,85)=7.88$, $p=0.0007$) and anatomical location ($F(2,85)=4.536$, $p=0.0134$)(**Fig. 3i**), with Tukey's post-hoc analyses determining these effects were driven by repeated blast-mTBI (sham vs 1x.: 444 mean dif. (-5150 to 6037, 95%CI), q=ns; sham vs. 3x: -8336 mean dif. (-13961 to -2711, 95%CI), q=0.0019).

Sleep impairment following TBI occurs in 30–65% of those with persistent PCS.[32,33] Interestingly, insomnia, which is characterized by difficulty initiating and maintaining sleep, is more common with less severe TBIs and blast-related mTBIs.[34-36] To measure changes in post-

traumatic sleep that are caused by blast-mTBI and that may contribute to the development of later sleep impairment, we used a noninvasive sleep monitoring system to record changes in the stereotypical sleep patterns of mice.[37,38] When measured seven days after blast-mTBI, the sleep bout duration and diurnal sleep-to-wake ratio of blast-mTBI mice was normal compared to sham control mice (**Fig. 3j, k**) and was consistent with previous reports of TBI mice one week after injury.[39] However, following a three-month period of recovery from repeated blast-mTBI, injured mice developed a statistically significant increase in sleep fragmentation characterized by a reduced average sleep bout duration and lower diurnal sleep:wake ratio (**Fig. 3j, k**) that was similar to clinical insomnia in humans. Thus, the development of sleep impairment occurs after the onset of microglial-associated pontine myelinopathy.

Myelin injury mediates sleep injury

We hypothesized a similar pathology would exist in the brainstem of military veterans with blast-mTBI. In a neuropathological analysis of autopsy subjects with (n=4) and without (n=4) blast-mTBI, phagocytic microglial nodules that highly express CD68 (i.e., microgliopathy; **Fig. 4a**) were often seen with internalized myelin (i.e., CNPase; **Fig. 4b**). Microglia nodules were identified in the brainstem and cerebellar white matter tracts of subjects up to 20 years after their last reported TBI. By observing IMC images stained with 6 antibodies specific for human protein targets, we confirmed that human microglial nodules were phagocytic and transcriptionally active (i.e., $CD68^{+}$, negative for histone 3 lysine 27 trimethylation) in contrast to the adjacent, uninvolved, normal-appearing microglia (**Fig. 4c**).

Insidious myelinopathy mediates several clinical diseases including multiple sclerosis, Parkinson's disease, and stroke and may contribute to the earliest occurring changes in age-

related cognitive decline and disability following TBI.[40] Our findings in mice indicate that diffuse axonal injury in the brainstem initiates latent white matter pathology that may drive the development of a spectrum of delayed-onset behavioral impairments related to mTBI. Diverse cognitive, behavioral, and somatic PCS occur in 77–97% of persons with repetitive TBI.[35,41] These persistent PCS develop over hours to months following injury[42] and may become chronic, lasting years.[43]

To determine whether brainstem white matter changes caused by diffuse axonal injury are associated with neurobehavioral symptoms in humans with blast-mTBI, we used magnetic resonance diffusion tensor imaging tractography (DTI) in living US veterans with repetitive blast-mTBI (n=20) and veterans deployed to the Iraq/Afghanistan war zones with no lifetime history of TBI (n=19). Subject demographics are provided in **Supplemental Table 3**. Guided by our animal model (**Fig. 3**), we reconstructed fiber tracts using the entire human pons as the seed region to avoid placement bias or error (**Fig. 4d**). Consistent with our observation of TBI-related myelin and neuronal injury in the pons of mice, TBI was associated with significant myelin injury of pontine fibers in veterans with mTBI via measures of DTI fractional, axial, and radial anisotropy (**Fig. 4e-g**). We next evaluated a possible dose-response between the number of blast-mTBIs and changes in pontine fractional anisotropy (FA) while controlling for the potential confounding variables of age and posttraumatic stress disorder (PTSD) symptom severity. Reductions in adjusted pons FA were associated with increasing numbers of self-reported blast-mTBIs (linear regression, $p<0.0001$; **Fig. 4h**).

Diverse functions are controlled by highly conserved brainstem circuits, including functions related to the common symptoms following mTBI: sleep structure, emotional state, and sensorimotor integration. To learn whether the development of these symptoms may be mediated

by changes in pontine white matter, we first evaluated the linear relation between age- and PTSD symptom severity-adjusted changes in pontine FA in all subjects and self-reported severity of persistent PCS related to mTBI as measured by the total score on an augmented Neurobehavioral Symptom Inventory (NSI+) questionnaire. Subjects rated symptom severities for dizziness, imbalance, dyscoordination; headache, nausea, vision, sensitivity to light; hearing, ringing in the ears, sensitivity to noise; numbness/tingling, changes in taste/smell; changes in appetite; changes in concentration, forgetfulness, decision-making difficulty, slowed thinking; fatigue, sleep impairment; anxiety, depression; irritability, poor frustration tolerance, getting into fights, disinhibition, mood swings; apathy/withdrawal; and slowness in speech ranging from 0 to 4 (not present, mild, moderate, moderately severe, severe) and symptom scores were summed (NSI+ total score). Using linear regression modeling, the relationship was highly significant (p<0.0001), indicating that greater total persistent PCS burden was associated with greater reductions in pontine FA (**Fig. 4i**). The number of lifetime mTBIs (log-10(x+1) transformed) similarly correlated with age- and PTSD symptom severity-adjusted measures of NSI+ total score (Spearman's r = 0.630, 0.5024 to 0.7308 95% CI; p=2.7 x 10^{-14}) indicating that total persistent PCS burden increases with the number of repeated mTBIs caused by blast exposure.

Lastly, we used statistical mediation analysis to evaluate the potential causal relationship between pontine white matter injury and persistent PCS burden. Using both pontine FA and NSI+ total scores adjusted for age and PTSD symptom severity, the regression coefficient between the number of blast-mTBIs and persistent PCS burden (i.e., the direct effect, DE) and the regression coefficient between pontine FA values and symptom burden were both significant (**Fig. 4j; Fig. S6a**). The indirect effect was (-0.006)*(-2715.00) = 16.3 (p<0.01). A validation analysis using nonparametric bootstrapping procedures determined that the effect size 95%

confidence interval ranged from 9.460 to 23.05 (**Fig. 4k**). The validated adjusted causal mediation was statistically significant (p=2 x 10^{-16}), supporting the conclusion that diverse persistent PCS following repetitive blast-mTBI are at least partially caused by pontine myelin injury. An identical mediation analysis determined a statistically significant relation between pontine FA and sleep impairment as measured by the Pittsburgh Sleep Quality Index (PSQI) total score similarly adjusted for age and PTSD symptom severity. Using a bootstrap-validated mediation analysis, both the adjusted causal mediation effect (ACME) and total effect (TE) were significant (ACME: 3.2 (1.991 - 4.75, 95% CI; p<0.0001); TE: 3.866 (2.254 - 5.56, 95% CI; p<0.0001)) (**Fig. 4l**). Taken together these results support the conclusion that chronic pontine myelin injury drives diverse persistent PCS following repeated blast-mTBI.

Discussion

We showed that brainstem nuclei are vulnerable to a single diffuse blast-mTBI. Within 15 minutes, we observed significant and consistent entry of blood-borne molecules into the brainstem parenchyma and highly variable entry into the cortex. One hour after mTBI, nearly 30% of experimental animals showed neuronal injury, seen as uptake of extravasated blood-borne dyes into axonal projections and cell bodies, whereas <5% of mice showed similar cellular injuries in the cortex. By four hours post-injury, nearly 50% of blast-mTBI mice showed cortical neuronal injuries. This suggests that a therapeutic window to prevent widespread cortical dissemination may exist in the initial 1 to 4 hours following blast-mTBI. Supported mechanisms include subtle neuroinflammatory processes that are likely critical determinants of brain-wide secondary injury, such as swelling of the brain. Such swelling develops within 14 days, is typically seen as significant ventricular enlargement, and is often mistaken for hydrocephalus.[46] However, when single mTBI-injured rodents are allowed to recover for a month, we found no overt microgliopathy or myelinopathy (**Fig. 3i**); this suggests that repeated injury is the key driver of these phenotypes.

The way in which repeated TBIs provoke the development of chronic pathology and persistent PCS is not well understood. We tested whether repeated diffuse mTBI causes the progressive disruption of brainstem structures responsible for changes in arousal and sensation. Using a data-driven approach, we agnostically identified injured areas by surveying the distribution of spatially-resolved, disease-associated microglial phenotypes across pontine nuclei. As expected, we observed that disease-associated microglia respond to neuronal and myelin injuries following the acute-injury patterns marked by microvascular extravasation and diffuse axon injury. We discovered, however, that release of oligodendroglial nuclear IL33 predicts the

regional density of disease-associated microglia, which can appear as single cells and small clusters, or "nodules", previously reported to facilitate the removal of degenerating axons and myelin.[31,47] Persisting pathologies of the pontine RF, first identified in our mouse model, were subsequently verified in living veterans with repeated blast-mTBI and in neuropathological studies in veterans with blast-mTBI from four independent laboratories.

We observed several highly stereotypical injury patterns to specific pontine nuclei following repeated blast-mTBI. Among these, a key brainstem area critical for good sleep hygiene is the pontine reticular formation. In living veterans with chronic repetitive blast-mTBI, the myelin integrity of the combined rostral and cerebellar pontine projections that were reconstructed by DTI tractography, were significantly correlated with the severity of persistent PCS including sleep impairment. Projections of the ascending RF strongly innervate central thalamic neurons[48,49] that modulate the depolarization and firing of neocortical circuits through input to the anterior forebrain mesocircuit and frontoparietal network.[50] These projections thereby affect the organization of goal-directed behaviors[50] and modulate arousal levels affecting cognition, stress, and sleep. [48,51,52] Likewise, the pontine projections to the cerebellum integrate cerebellar function with diverse brainstem nuclei, including most raphé nuclei, the locus coeruleus, the pedunculopontine nucleus, and several segments of the RF.[53] Although lesions and DTI abnormalities of the SCP have been frequently reported across a variety of TBI mechanisms of injury and severity of TBI,[17,54,55] their role in the development of persistent PCS remains unknown. What is known is that experimental lesions of the SCP in cats result in nightly sleep loss,[56] whereas cerebellectomized cats display increased drowsiness without sleep loss;[57] this suggests that the prominent cerebellar injuries caused by TBI may also be a significant source of sleep morbidity. Lastly, in keeping with our hypothesis that pontine myelin injury is a causal

mediator of persistent PCS, as opposed to the injury of specific output tracts which were not declared *a priori*, we did not evaluate the individual contributions of rostral versus cerebellar projections. Subsequent study is needed to determine the relative contributions of TBI-induced injuries to the SCP versus the pontothalamic projections in the development of persistent PCS, since each may pose unique diagnostic and interventional opportunities. Taken together, the results of this study indicate that diffuse traumatic brain injuries caused by blast overpressures may provoke common, though diverse, neurobehavioral symptoms caused by chronic pontine white matter injuries in nuclei subserving their function.

Methods

Study Design

The aim of this study was to determine the frequency and pattern of diffuse axonal and white matter injury in the brainstem following blast-mTBI and to evaluate its relationship with common persistent PCS in both a mouse model of diffuse blast-mTBI with attenuated head movement and in military veterans with history of blast mTBI. Blast exposures occur from all directions, and may not be accompanied by any focal blunt force trauma. This study in a military veteran cohort with primarily repetitive blast-mTBI enabled us to examine the effect of repetitive diffuse blast mTBI on the relationship between brainstem structure and persistent PCS that may be generalizable across mTBI without the confounds associated with excessive head movement, which is well established to injure brainstem centers following TBI caused by diverse forms of trauma.

A total of 39 male veterans reporting from 0 to 102 blast-induced mTBIs were studied. Although female veterans were eligible for study inclusion, none enrolled. Study inclusion

criteria included documented military service in Iraq and/or Afghanistan with the US Armed Forces during Operations Enduring Freedom, Iraqi Freedom, and/or New Dawn. Veterans meeting VA/Department of Defense/American Congress of Rehabilitation Medicine criteria for mTBI following at least one blast exposure were included in the TBI group.

Exclusion criteria for the study included a history of moderate to severe TBI, seizure disorder, insulin-dependent diabetes, DSM-IV diagnosis of alcohol or other substance use disorder**,** dementia, bipolar affective disorder, and psychotic disorders. Subjects using medications likely to affect cognitive or behavioral assessments, such as opiates, benzodiazepines, and sedating antihistamines, were also excluded. MRIs were contraindicated for veterans with retained shrapnel or other metal objects, who were thus excluded from MRI.

A total of 232 male wild-type C57BL/6J, 20 $Cx3cr1^{EGFP}/CCR2^{RFP}$ and 15 $Cx3cr1tm2.1^{cre/ERT2}/ Rpl22tm1.1^{Psam/J}$ mice age 3 to 6 months were studied. Mice were randomly assigned to either TBI or sham control groups. Group sizes were based on pathology in this and other established TBI models.[17,58-60] In each experiment, mice from the control and TBI groups were analyzed under identical conditions.

Human subjects

Human studies were approved by the VA Puget Sound Health Care System Institutional Review Board. All living veteran participants provided written informed consent prior to any study procedures. The study conformed to institutional regulatory guidelines and principles of human subject protections in the Declaration of Helsinki. Veterans with and without mild TBI were characterized by physical, neurological, and behavioral examinations that included assessments for PTSD using the PTSD Checklist-Military version total score, for sleep disturbance using the

PSQI total score, and for current post-concussive symptoms using the Likert-scaled NSI+ symptom questionnaire. The NSI+, based on the standard NSI, is a self-report instrument consisting of the base 22 NSI questions plus the following six TBI-associated PCS: 1) disinhibition, 2) apathy/withdrawal, 3) ringing in the ears, 4) mood swings, 5) getting into fights, and 6) slowness in speech. Responses are scored on scale of 0-4; (0) None, (1) Mild, (2) Moderate, (3) Severe, and (4) Very Severe. The Structured Clinical Interview for DSM-IV was used to establish diagnoses of Axis I psychiatric disorders. A lifetime history of TBI was obtained using a semi-structured TBI interview performed by two expert TBI clinicians simultaneously.[61] Magnetic resonance DTI was performed within 3 months of clinical evaluation.

Clinical neuropathology

Human donor research brain specimens and their related clinical/exposure information were collected and used as de-identified materials in accordance with procedures approved, as appropriate, by the VA Puget Sound Health Care System, University of Washington, and the Uniformed Services University Institutional Review Boards. Tissue samples were obtained from brains donated, with informed consent by their legal next of kin, of veterans with a history of mTBI caused by blast exposure and control subjects matched by age and sex but without a lifetime history of TBI. Formalin fixed paraffin embedded (FFPE)-brain sections were de-paraffinized and rehydrated using previously described procedures,[17] blocked in 10% normal goat serum (1 hour at room temperature), and stained overnight at 4°C using the following antibodies: rabbit polyclonal anti-GFAP (Abcam, Burlingame, CA; 1:1,000), mouse monoclonal anti-Iba-1 (Wako Chemicals, Richmond, VA; 1:1,000), or mouse anti-CD68 (Agilent, Santa

Clara, CA; 1:100). Heat-mediated antigen retrieval was performed in citrate buffer (pH 8.0; 80°C) for 30 minutes and then cooled to room temperature before further use. Stained slides were mounted with ProLong Diamond antifade mountant (ThermoFisher Sci, Waltham, MA).

Diffusion Tensor Imaging (DTI)

Magnetic resonance DTI was performed using an established protocol[17,61] on a 3.0 T Philips Achieva whole-body scanner (Philips Medical Systems, Best, Netherlands) equipped with a 32-channel radiofrequency head coil. Briefly, images were acquired using a single-shot spin-echo echo-planar sequence with TR=10.76 sec; TE=93.5 msec; flip angle=80 degrees; matrix size=128•128; field-of-view (FOV)=256•256; slice thickness=2mm; 64 gradient directions; and b-factors=0 and 3,000s/mm2.

Images were preprocessed to correct for head motion, eddy current, and B0-field inhomogeneity-induced geometric distortion using the Oxford FMRI Software Library (FSL) DTI toolbox. Image slices with large within-slice intensity differences, wrapping abnormalities, or other artifacts were identified by analysis with DTIPrep and subsequently removed. DTI tractography was used to test for correlations between DTI parameters, the number of reported TBIs, and symptom areas related to known brainstem functions. To conduct tractography, DICOM-formatted diffusion images were converted to nrrd data file/header (nhdr) format (http://teem.sourceforge.net/nrrd/format.html) in g-Fortran. Fiber tracts were created in SLICER 4.3.1 (http://www.slicer.org/). After the diffusion data were loaded into Slicer in nhdr format, tensor estimates were created by converting the diffusion weights.

The resulting process created scalar measurements that were used to create corresponding images of FA. The Editor module in Slicer was used to create a label map and a region of interest

(ROI) located in the four ROIs in the pons (**Fig. 4d**). Fiber tracts for each individual participant were reconstructed from these seed regions using 1mm spacing thresholds, and the resulting fiber tract vtk file was read into g-Fortran for quantitation of FA, mean diffusivity, radial diffusivity, and axial diffusivity. These values were analyzed using nonparametric Spearman correlation statistical analysis with respect to the log10(number of reported TBIs + 1), hours of self-reported nightly sleep, and other symptoms (**Fig. 4**), with final reported p-values controlled for multiple comparisons using a rigorous 1% false discovery rate (FDR) adjustment. Each volume of interest (VOI) had a volume of approximately 20mm^3 and was manually positioned. Evaluation of pontine DTI averaged bilateral VOIs for rostral pontine (RP) and pontocerebellar (PC) tracts with Montreal Neurologic Institute atlas x, y, z coordinates of (Left RP [-27.1, -20.0, -6.0]), (Right RP [5.0, -20.0, -6.0]), (Left PC [-30.0, -38.0, -33.0]), and (Right PC [5.0, -38.0, -33.0]; exemplars are found as white boxes in **Fig. 4d**).

Animals

Mice used in this study comprised group-housed, 3-to-6-month-old male C57Bl/6J wildtype, Cx3cr1^{EGFP}/CCR2^{RFP} [B6.129(Cg)-Cx3cr1tm1Litt-Ccr2tm2.1Ifc/JernJ (JAX stock # 032127)], and microglial RiboTag mice [heterozygous offspring of B6.129P2(C)-Cx3cr1tm2.1(cre/ERT2) mice (JAX stock # 020940)] crossed with RiboTag flox mice (JAX stock # 011029 B6N.129-Rpl22tm1.1Psam/J)). Animals were maintained on a 12-hour light/dark cycle with *ad libitum* food and water access. All study procedures were in accordance with Association for Assessment and Accreditation of Laboratory Animal Care guidelines and approved by the VA Puget Sound Health Care System Institutional Animal Care and Use Committee.

Modeling blast overpressure

TBI was modeled with a shock tube designed to simulate open-field blast explosions (Baker Engineering and Risk Consultants, San Antonio, TX) as described elsewhere.[12,17] Briefly, anesthetized mice were maintained on a non-rebreathing anesthesia apparatus (2% isoflurane in 1 Lpm oxygen) while secured on a gurney with their ventral side oriented toward the oncoming blast overpressure wave and then placed into the shock tube. TBI mice were paired with sham control mice and both were similarly secured in the shock tube while under anesthesia for an identical amount of time. Mice received blast or sham procedures once per day, with 3x treatment mice receiving one treatment per day for three days. The mean overpressure wave characteristics for 102 blast overpressure waveforms generated in this experiment are 20.62+/-0.15psi; 5.65+/-0.036ms; 0.038+/-0.00019psi·ms, including peak intensity (psi), initial pulse duration (ms), and impulse (psi·ms), respectively. **Figure S2** displays an average of waveforms from the study; this image, taken at random, consists of 102 overpressures and is consistent with the accepted properties of mild to moderate blast exposure,[17,62,63] resulting in a >95% survival rate. After TBI and sham exposures, mice were monitored and generally regained normal appearance within 4 hours of exposure.

Tamoxifen treatments

Three weeks after TBI or sham treatments, gene recombination was induced in microglial RiboTag mice by two i.p. injections of tamoxifen (4mg in 200µl corn oil [Sigma, St. Louis, MO; C8267]) that were administered two days apart.

RiboTag immunoprecipitation

Tamoxifen-treated Cx3cr1creER-Rpl22 RiboTag mice were deeply anesthetized with a lethal injection of sodium pentobarbital (210 mg/kg, i.p.) followed by transcardial perfusion with PBS-containing cycloheximide (100μg/ml). Brains were removed; subdissected on ice into brainstem, cerebellum, and cortical hemisections; weighed; flash frozen; and stored at -80°C until used. Upon use, approximately 20 to 30mg of each frozen tissue was cut and collected into RNase-free tubes followed by homogenization by hand with a tube-fitting disposable pestle using 2-3% weight per volume of the following buffer (HB-S): DTT (Sigma, St. Louis, MO; 646563, 1mM), Protease Inhibitor Cocktail (Sigma, St. Louis, MO; P8340, 1x), RNAsin (Promega, Madison, WI; N261B, 200 units/ml), cyclohexamide (Sigma, St. Louis, MO; C7698, 100μg/ml), heparin (Sigma, St. Louis, MO; H3393, 100 mg/ml) in RNase-free deionized water. Homogenized samples were centrifuge-clarified (12,000 x g, 10min, 4°C), and supernatants were transferred into fresh RNase-free tubes followed by incubation (4°C for 4 hours with tube rotation) with mouse monoclonal anti-HA.11 (Covance, MMS-101R, 3 uL/sample). After 4 hours, 200uL of Protein A/G Magnetic Beads (Promega, Madison, WI; 88803) were added to each sample and rotated at 4°C overnight. Beads were washed and pre-equilibrated in homogenization buffer and blocked with 4% bovine serum albumin (Sigma, St. Louis, MO; 3117332001) for 1 hour prior to use. The next day, mRNA transcripts and their associated antibody-bound ribosomes were precipitated by magnet and washed (3 x 15 minutes each, 4°C with rotation) in 1 ml high salt buffer (500 mM Tris pH 7.4, 300 mM KCl, 12 mM $MgCl_2$ 1% NP-40, 1 mM DTT, 100 μg/ml cyclohexamide in RNase-free water). Immediately after the final wash, transcripts were dissociated from their precipitating complexes by addition of RLT Buffer (Qiagen, Germantown, MD; 79216) supplemented with 10 μl/ml RNase-free β-mercaptoethanol (Sigma, St. Louis, MO; 63689). RNA was purified by RNeasy Plus Micro kit (Qiagen, Germantown, MD; 74034)

according to manufacturer's protocol, followed by RNA quantification using a Nanodrop spectrophotometer (Thermofisher Sci, Waltham, MA). cDNA of precipitated transcripts was made using the SuperScript VILO cDNA synthesis kit (Thermofisher, Waltham, MA; 11754050) according to the manufacturer's protocol. Yield of cDNA preparations was determined by nanodrop (input: ~5ng/µl; immunoprecipitant: ~1.5-2.5 ng/µl). To verify enrichment of mouse microglial genes, immunoprecipitants were analyzed in triplicate by real-time PCR on a StepOnePlus Real-Time PCR System (Thermofisher, Waltham, MA), using KAPA Universal SYBR Green master mix and the following primers: Aif1(NM019467.3) forward 5'-GGATTTGCAGGGAGGAAAAG, reverse 5'-TGGGATCATCGAGGAATTG; NTRK2 (NM008745.3) forward 5'-TGTTGCCTATCCCAGGAAGTG, reverse 5'-CTGCAGACATCCTCGGAGATTA; GFAP (NM010277) forward 5'-ACCATTCCTGTACAGACTTTCTCC, reverse 5'-AGTCTTTACCACGATGTTCCTCTT; GAPDH (NM008084) forward 5'-CTGCACCACCAACTGCTTAG, reverse 5'-ACAGTCTTCTGGGTGGCA GT. Representative results are shown in **Figure S3**.

The following thermocycler settings were used: 95°C for 20 seconds followed by 40 cycles of denaturation (95°C for 3 seconds), primer annealing and extension (60°C, 30 seconds) followed by a melting curve. Gene expression was normalized within subjects to GAPDH levels and quantified using the $2^{-\Delta\Delta CT}$ method. ROX was used as a reference dye.

mRNA preparation and analysis

RiboTag-immunoprecipitated mRNA was ribosomal RNA depleted using the Ribo Zero Gold Magnetic system (Epicenter/Illumina, San Diego, CA). We prepared RNA-sequencing libraries using ScriptSeq v2 kit (Epicenter) followed by single-end sequencing (1x50bp) on an Illumina

HiSeq 2500, generating 4×10^6 mean reads per sample. RNA-seq fastq files were aligned to the mouse genome build *mm10* with *STAR* aligner and processed into transcript-level summaries using the expectation maximization algorithm *RSEM*. Transcript-level summaries were combined into gene-level summaries by adding all transcript counts from the same gene. Gene counts were normalized across samples using *RLE* normalization, and the gene list was filtered based on mean $\log_2$ (counts per million reads) > 4 in at least 3 samples in any group, which left about 14,000 "detected" genes for further analysis. Consistency of replicates was inspected by principal component analysis using *R*. Differential expression was assessed through sequential analyses of both an initial discovery cohort to identify candidate genes (α=0.05) and a secondary validation cohort (α=0.05). The candidate differential genes, defined as the shared set of overlapping genes, was further evaluated. Forty-percent of the identified candidate differentially expressed genes have been previously reported (**Table S1**).

Gene set enrichment analysis (GSEA) was conducted in DAVID (https://david.ncifcrf.gov/tools.jsp) using the full list of candidate differentially expressed genes for brainstem. Official gene symbols were queried against the *Mus musculus* species using the default settings for analyses conducted by DAVID. Gene Ontology terms with Benjamini-corrected p<0.05 were reported.

Data availability

Data are available through reasonable requests addressed to the corresponding author.

Neurovascular permeability studies

Radiolabeled tracer preparation: Albumin (Sigma, St. Louis MO) was radiolabeled using established protocols[64] with ^{99m}Tc (GE Healthcare, Piscataway, NJ). Hydrochloric acid was used to pH-adjust a solution of aqueous stannous tartrate (240 mg/ml) and albumin (1 mg/ml) to a final pH of 3.0 before the addition of one millicurie of ^{99m}Tc-NaOH4 to the mixture, which was then allowed to react for 20 min. The resulting radiolabeled ^{99m}Tc-albumin was column-purified (G-10 Sephadex; GE Healthcare, Piscataway, NJ) in 0.1 ml fractions of phosphate buffer (250 mM). Purified ^{99m}Tc-albumin was > 90% acid precipitable in 1% bovine serum albumin and trichloroacetic acid (30%) (1:1 mixture). Each mouse was administered 5×10^6 counts per minute (cpm) of purified ^{99m}Tc-albumin fraction in 0.2 ml lactated Ringer's solution containing 1% BSA. ^{14}C-sucrose was supplied as an ethanol-dissolved product (GE Healthcare, Piscataway, NJ). Ethanol was evaporated before use and resuspended at 1 x 10^7 cpm in 1% BSA lactated Ringer's solution. Radiolabeled tracer injections: At 15 minutes, 24 hours, or 72 hours after mTBI or sham treatments, mice were anesthetized with urethane (4 g/kg; 0.2 ml; i.p.) followed by exposure of the jugular vein and injection with ^{14}C-sucrose or ^{99m}Tc-albumin in 0.2 ml of lactated Ringer's solution with 1% BSA for 10 minutes. The descending abdominal aorta was cut to collect blood. Vascular contents of the brain were cleared by left cardioventricular perfusion (20 ml lactated Ringer's solution per minute) after clamping the descending thoracic aorta and severing both jugular veins. Two brains with incomplete blood washout were excluded from analysis. After perfusion, the brain was removed; subdissected into cortical hemispheres, brainstem, and cerebellum; and individually weighed. The analytical results of these experiments with respect to cerebellum were recently published by our group.[64] Radioactivity was calculated as cpm/g tissue or cpm/ml serum, as appropriate. The brain tissue radioactivity was then divided by the corresponding serum radioactivity to yield units of microliters/gram of brain tissue.

In vivo dextran labeling of injured cells

Extravasation of blood-borne dextran to label coincident vascular and neural injury was accomplished as described elsewhere.[17] Briefly, following induction of isoflurane anesthesia prior to TBI or sham procedures, mice were injected with 100 µl of 400 mg/ml 10kDa dextran labeled with tetramethylrhodamine (Life Technology, Grand Island, NY) into the retro-orbital sinus. After TBI or sham treatments, mice then recovered for 1 or 4 hours before euthanasia and transcardial perfusion with phosphate-buffered saline followed by 4% formalin.

Animal MRI

MR imaging was acquired on 12 mice (6 sham and 6 single mTBI) at 24 hours post-injury and again at 30 days post-injury. Mice were anesthetized with isoflurane and scanned over the entire brain using a high-resolution 14 T MRI (Avance III, vertical bore, Bruker BioSpin Corp, Billerica, MA). T2 quantitative mapping (T2) was acquired with a voxel size of 0.12 x 0.12 x 1.0 mm^3, 15 slices, TR 1⁄4 2000 ms,16 echoes, spacing: 6.7 ms, TE Effective 1: 6.7 ms, TE Effective 2: 13.4 ms, and was used to measure ventricular volume and scan for evidence of parenchymal bleeding within visible areas. All analyses were performed by a blinded investigator (DJC). Analysis of T2 quantitative maps required threshold bounding set from 36 to 200, which included ROIs but excluded normal cortex and white matter. Manually drawn ROI analysis was performed using Image J software. ROIs included the volume of voxels within the threshold boundary comprising the lateral, 3rd, and 4th ventricles, across a total of seven image slices, and total volumes were calculated by multiplying with voxel size in mm^3.

Mouse sleep assessments

639 Noninvasive measurements of sleep bout duration and the sleep:wake ratio were acquired using
640 an automated sleep/wake scoring system designed for rodents (PiezoSleep; Signal Solutions,
641 Lexington, KY). One week after the final TBI or sham procedure and again three months later,
642 mice were placed in open-floored chambers installed with piezoelectric sensors are designed to
643 detect and track the previously characterized sleep activity of mice.[65] Mice were allowed to
644 acclimate for 2 days before their undisturbed activity was recorded over the next 3 days
645 following previously established methods.[37,66] Data were analyzed using the Sleep Statistics
646 Toolbox (Signal Solutions, Lexington, KY).
647
648 **Microscopy**
649 Microscopy was performed as described elsewhere.[17] Briefly, brains were post-fixed in 10%
650 neutral buffered formalin at 4°C for 3 to 5 days followed by 24 hours of equilibration in 30%
651 sucrose/PBS prior to embedding in OCT (Tissue-Tek, Torrance, CA). Antigen retrieval was
652 performed using 50 mM of sodium citrate (pH 8.0) with heat (80°C, 30 min). Cryopreserved
653 floating tissue sections were permeabilized with 1% Tx-100 (Sigma, St. Louis, MO), blocked
654 with 10% bovine serum albumin (1 hour, room temperature), and immunostained and mounted
655 using Prolong Gold Antifade Reagent (Thermofisher, Waltham, MA). The following antibodies
656 were used overnight at 4°C: mouse anti-CNPase clone SMI-91 (Biolegend, Dedham, MA;
657 1:1,000), astrocyte marker anti-GFAP (Millipore, Billerica, ME; 1:1000), neuronal marker anti-
658 neurofilament-heavy chain (Nf-HC) (Aves, Tigard, OR; 1:1000), mouse monoclonal TauC3
659 (ThermoFisher, Waltham, MA; 1:1000), rabbit anti-phospho Tau 396 (AnaSpec, Freemont, CA;
660 1:1000), and mouse monoclonal anti-Iba-1 (Wako Chemicals, Richmond, VA; 1:1,000).
661 Corresponding secondary antibodies were applied for 2 hours at room temperature (Jackson

Immunoresearch, West Grove, PA; 1:1,000). Confocal microscopy was performed with a Leica TCS SP5 II with tunable emission gating. Representative brainstem regions imaged for analyses are identified in **Supplemental Figure 5**. To quantify the degree of myelin internalization by microglia, z-plane images of tissue areas (approximately 600 μm x 600 μm x 50 μm) were acquired by performing sequential, between-stack, single-photon excitation at 488 nm and 543 nm using system optimized stepping (~2 μm). Images were acquired with the Leica Application Suite and processed using linear contrast and brightness adjustments applied identically and simultaneously to all data being directly compared within each experiment.

Imaging mass cytometry

Metal-conjugated antibodies were either purchased (Standard Biotools, San Francisco, CA) or custom-made by conjugation using the MaxPar X8 labelling kit (Standard Biotools, San Francisco, CA) and carrier and preservative-free antibody formulations following the manufacturer protocol. Typical antibody recovery was 59 ± 0.16%. Tissue staining with metal-labeled antibodies was similarly accomplished using the manufacturer's protocol for formalin-fixed paraffin-embedded slides with minor modifications. Briefly, tissue sections of either formalin-fixed human paraffin embedded tissues or covalently bound, agarose-block embedded mouse brain sections were used for imaging mass cytometry. Paraffin embedding and sectioning followed standard histological procedures, whereas preparation of agarose-block embedded brains followed procedures developed and published by the Allen Institute for Brain Science for use in serial two-photon tissue tomography (dx.doi.org/10.17504/protocols.io.bf65jrg6). One each TBI and sham mouse brain were randomly paired and embedded together into the agarose block. The brains were oriented in parallel such that the sham brain cortex was always oriented

685 facing outward. Agarose block–embedded sections were cut at 50 µm thickness (immediately
686 after aqueous two-photon imaging). Slices cut from agarose block–embedded brains were
687 robotically mounted with a TissueVision 1600FC SlicerPlacer module (Tissuecyte, Newton,
688 MA) onto superfrost plus slides (Thermo Fisher Scientific Bothell, WA) and subsequently air-
689 dried for up to one year before use. DNA intercalator (Iridium 191/193, 201192B; Standard
690 Biotools, San Francisco, CA) was diluted 1:4000 in Dulbecco's phosphate buffered saline
691 (21600-051, in 18.2 MΩ water; Thermo Fisher Scientific; Bothell, WA) for 30 minutes at room
692 temperature before slides were washed in 18.2 MΩ water, air-dried overnight, and stored at room
693 temperature until used.

694 Coronal brainstem hemisections were routinely ablated using the Hyperion UV laser
695 system with 1 μm^2 diameter (Standard Biotools, San Francisco, CA). The ablated materials are
696 carried by helium into the Helios mass cytometer, which uses a time-of-flight mass detector to
697 detect and timestamp the abundance of a user-defined mass range for each rasterized 2-
698 dimensional location.[67] The Hyperion instrument was tuned daily according to the
699 manufacturer's protocol.

700

701 **Single cell gating, analysis, and image visualization**

702 Imaging mass cytometry datasets were collected in MCD file format and exported as single
703 channel TIFs for bulk import into CellProfiler. There, segmentation of single cells based on the
704 watershed gradient algorithm using DNA intercalator channels (191Ir, 193Ir) and a proprietary
705 mix of plasma membrane markers (channels 195Pt, 196Pt, 198Pt; IMC Cell Segmentation Kit,
706 TIS-00001; Standard Biotools, San Francisco, CA) was performed to define cell nuclei and
707 single cell boundaries, respectively. Microglia were gated by selecting cells with marker

intensities for CCR2$^-$(<2.5) and Iba1$^+$ (> 6) to delineate them from peripheral immune cells expressing higher levels of CCR2. DAMs were gated by selecting the following parameters: Iba1 > 6, CD68 > 10, CCR2 < 2.5, ApoE > 8, and CD63 >2. The thresholds for CCR2, ApoE, and CD63 positive signals was determined by comparison of the CD63+ microglial cells that were identified by manual observation, relative to other cell types. The threshold for CD68 high or low signal was determined by the comparison to manually identified microglia in sham control animals establishing the lower limit. All major cell types, including astrocytes, neurons, oligodendrocytes, peripheral immune cells, and vascular endothelium, were validated by manual annotation.

Brainstem images were aligned to the Allen mouse brain reference map[68] and segmented by anatomical region in HistoCAT.[69] Using HistoCAT, Barnes-Hut t-SNE, and phenograph, neighborhood analyses (using a proximity of 6) were conducted using default settings. Images representing single and merged channels, such as **Fig. 2f**, were saved as TIF files via MCD viewer software (Fluidigm), imported into Adobe Photoshop 2021 (Adobe Systems, San Jose, CA), and processed with a Gaussian blur filter to de-speckle images. Afterward, all images being directly compared within a figure panel were uniformly and simultaneously adjusted to optimal brightness and contrast levels using a single adjustment mask.

Western blot analyses

Brains were dissected in PBS on ice. Protein lysates were prepared as described elsewhere.[17] Briefly, phosphatase inhibitor cocktail sets 2 and 3 (Sigma, St. Louis, MO) were added (10 µl/ml) to lysis buffer, and tissues were homogenized twice by hand using an Eppendorf tube-fitting pestle (Eppendorf, Hauppauge, NY) before centrifuge clarification at 12,000xg for 10

minutes. TGX Criterion 4-20% SDS-polyacrylamide gels (Bio-Rad, Hercules, CA) were loaded with 20 μg protein per lane using supernatants of the clarified lysates from individual animals. Membranes were then blocked with 10% nonfat milk (1 hour at room temperature) and probed with antibodies recognizing the following targets: anti-pathological tau clones AT8 and AT270 (Thermo Fisher Scientific, Rockford, IL); anti-mouse tau (total) clone Tau5 and anti-phospho Tau S396 (Life Technologies, Grand Island, NY); MOBP (Genetex, Irvine, CA); CNPase (Biolegend, San Diego, CA); mouse anti-MBP and rabbit antibodies anti-LINGO1, anti-GFAP, and anti-MnSOD (EMD-Millipore, Billerica, MA); and Pyruvate kinase (Rockland, Gilbertsville, PA). Probes for the load control protein, pyruvate kinase, were conducted after stripping.

Causal mediation analysis

Mediation analysis evaluates the statistical probability of a known third (declared) variable to mediate the primary relationship between independent and dependent variables. The effect of changes in pontine FA (adjusted for age and PCL-M total scores for PTSD symptom severity) to mediate behavioral and physiological symptoms (dependent variables) following self-reported TBI (independent variable) was first evaluated with multivariable linear regression in R (**Fig. 4j**). A subsequent validation analysis was conducted with the R statistical package Mediate using nonparametric bootstrapping procedures and also used age- and PTSD symptom severity-adjusted pontine FA (**Fig. 4k**). This indirect effect is measured as the portion of the relationship between two variables mediated by the third variable.[70,71] In validation analyses, unstandardized indirect effects were computed thrice for each of 10,000 bootstrapped samples, and the 95% confidence interval was computed by determining the indirect effects at the 2.5th and 97.5th percentiles. Sensitivity analyses were conducted in R and are illustrated in **Figure S5**.

Statistical analyses

Data are presented as distributions (violin plots) or mean ± standard error of the mean (bar graphs). Multivariable linear regression: Standard analysis of variance (ANOVA) was used for planned statistical tests involving multiple measures or groups. False discovery rate-adjusted post-hoc analyses with alpha = 0.05 were conducted as indicated. T-tests were used for planned comparisons involving two normally distributed groups, with nonparametric Mann-Whitney tests used for unpaired comparison of non-normal distributed groups. Bivariate linear or simple linear regression was used to predict DAM frequency based on IL-33 expression. Multivariate linear regression analysis reported correlations adjusted for age, depression, PTSD symptom severity, sleep apnea, and alcohol use. Statistical significance was defined as $p \leq 0.05$. Sample sizes were based on previous reports.[17,60,72] All analyses were determined using Prism 8.4 (GraphPad, San Diego, CA), SPSS software (IBM, Armonk, NY), or R version 3.6.1 (R Core Team, Vienna, Austria).

Acknowledgments

Author contributions

JSM: Conceptualization, formal analysis, supervision, funding acquisition, investigation, visualization, writing—all drafts, writing—review and editing; AGS, MMC, AFL, CM, AC, JRP, AS-D, and RGT, KFP, DAM, CDK: Formal analysis, investigation; MY: Validation; TLR and KDM: Formal analysis, performed the DTI analyses; DJC and DGC, DRM, JWR, MO: Investigation; DPP, WAB, JPM, MAR, EAC, CLS, CDK, DAM and ERP: Conceptualization, resources.

We'd like to thank Dr. Erica Melief and Aimee Schantz for outstanding administrative support, and Lisa Keene, Amanda Keen, and Katelyn Kern for expert technical assistance, and the incredible generosity of the military Veteran and civilian participants, and their families, without whom this work would be impossible.

Funding

This study was supported by the Veterans Affairs Office of Biomedical Laboratory Research & Development (JSM, I01BX004896; DGC, I01BX002311; AGS, 1IK2BX003258), VA Rehabilitation Research & Development (ERP, I01RX000521, I01RX001612, I01RX003087), VA Puget Sound R&D Seed grant (JSM), University of Washington Friends of Alzheimer's Research (DGC, ERP), UW Royalty Research Fund (DGC), and the Northwest Network Mental Illness Research, Education, and Clinical Center (JSM, MAR, ERP). Human brain tissue specimens were derived from the Uniformed Services University neuropathology repository (D.P.), University of Washington BioRepository and Integrated Neuropathology (BRaIN) Laboratory with support from the Nancy and Buster Alvord Endowment (to C.D.K.), the Henry Jackson Foundation, and the Neuropathology Core of the UW Alzheimer's Disease Research Center (P30 AG066509).

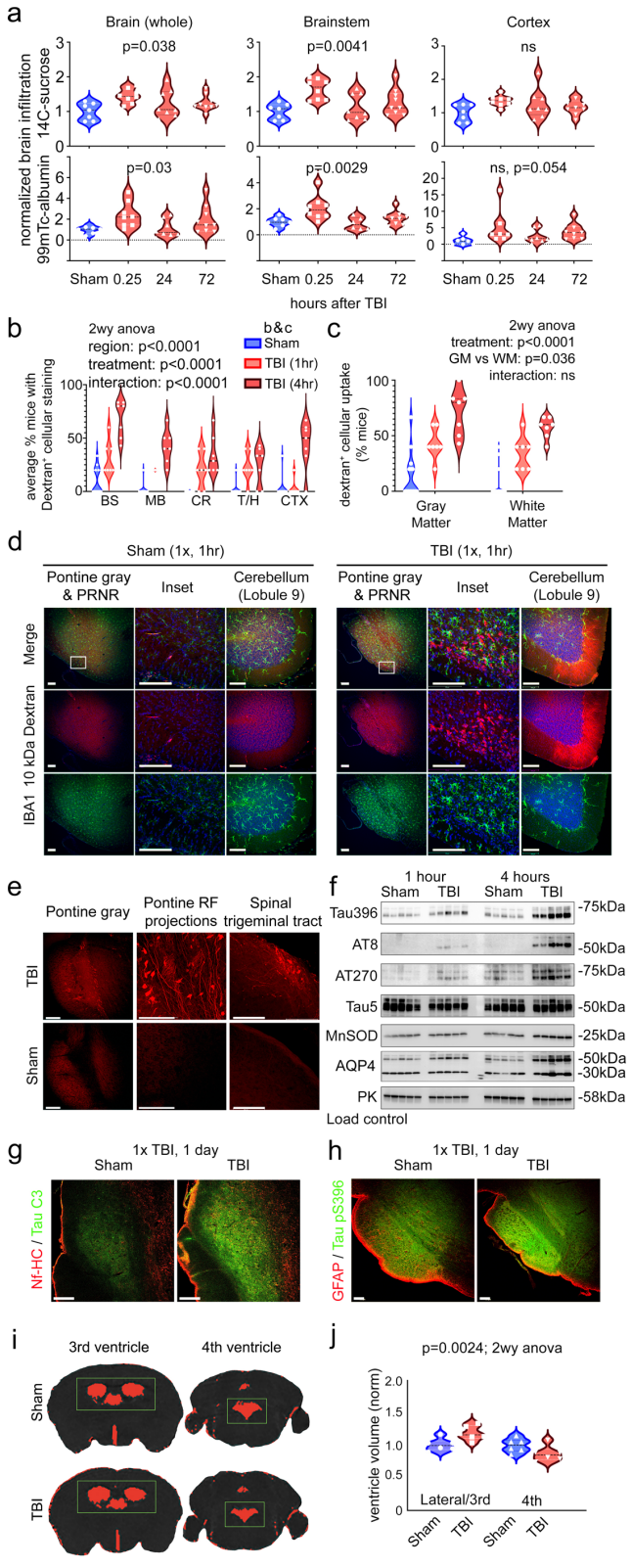

Figure 1. Pontine nuclei are vulnerable to a single blast mTBI. a, Time course and quantitation of blood-borne small (^{14}C-sucrose) and large (^{99m}Tc-albumin) molecule extravasation into brainstem, cortex, and whole brain. **b,** Time course and distribution of injured neurons labeled with a blood-borne fluorescent dye as observed using confocal microscopy. **c,** Injured cell distributions viewed across white vs. gray matter. (**b**) and (**c**) show the average number of animals per experiment with labeled cells (mice, 1 hr: N=35,35; 4 hr: N=40,40; average ~5 mice per group per cohort; 7 cohorts). **d,** Representative micrographs of injured, dye-labeled neurons and accompanying microglial response 1 hr following TBI. Staining of injured pontine cells is subtle compared to cerebellar Purkinje cells. PRNR, rostral pontine reticular nucleus. **e,** Example micrographs of injured locations often observed. RF, reticular formation. **f,** Western blots document increasing tauopathy (Tau396, AT8, AT270; axon injury markers) and gliovascular injury (aqp4) during the 1-4 hr acute inflammatory phase after a single diffuse mTBI (5 mice/group). Tau5, total tau; PK, pyruvate kinase (load control). **g** and **h,** Confocal micrographs of (**g**) caspase-cleaved Tau (Tau C3) and (**h**) pathologically associated tau hyperphosphorylation (pS396) in the pons 1 day after TBI. **i,** Representative T2 MRI of mice 24 hrs after a single TBI or sham procedure. Red color indicates pixels that exceed the threshold value (representative of CSF) and green is the region-of-interest (ROI) bounding box. **j,** Quantification of ventricle volumes (6 mice/group). One-way ANOVA (**a**), two-way ANOVA (**c, j**), and mixed effects model (**b**). Scale bars are 100μm.

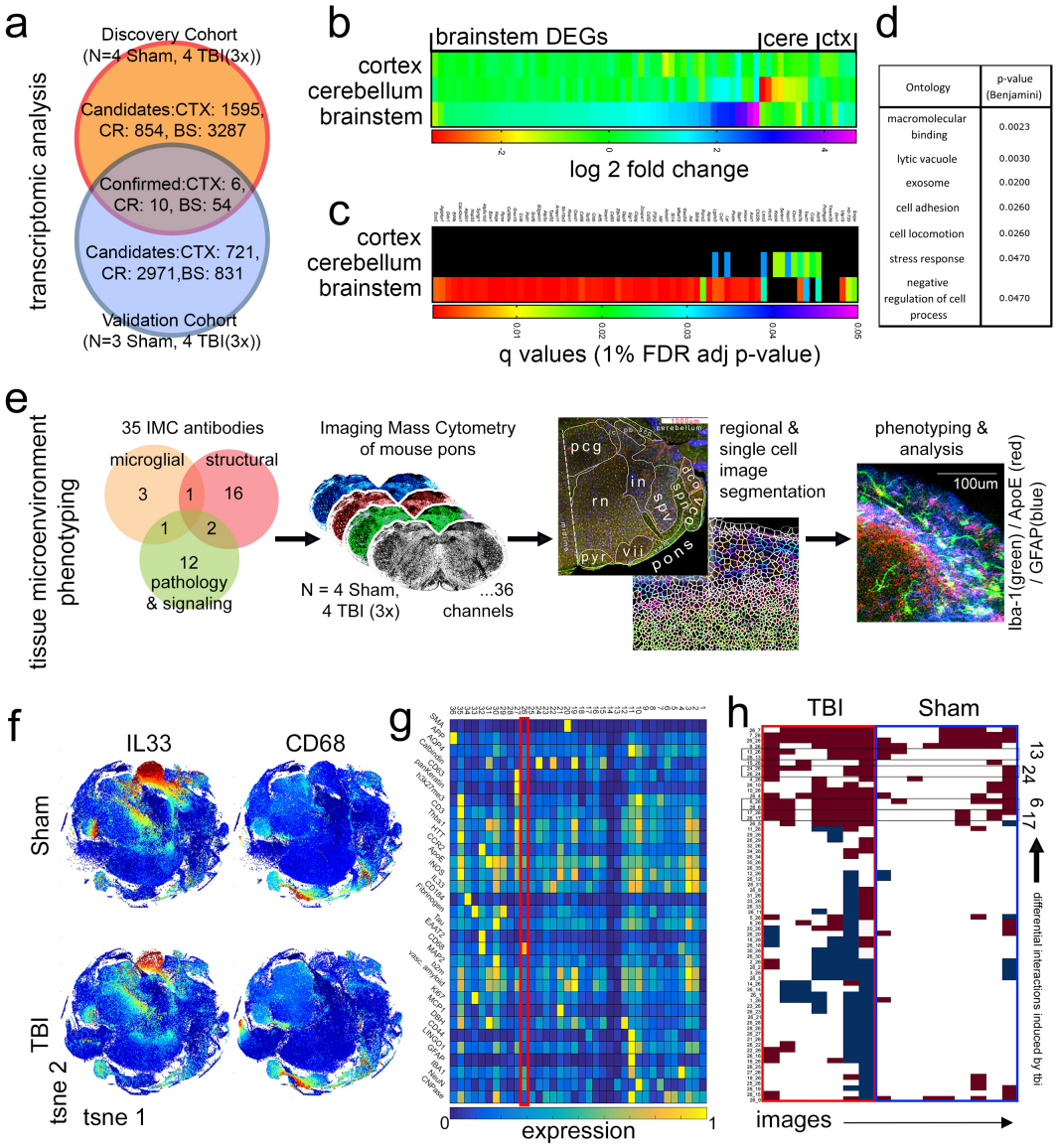

Figure 2. mTBI induces persistent pontine microgliopathy. a, Discovery and validation strategy using 3-month-old male Cx3cr1^{CreER}:Rpl22^{HA} RiboTag mice to identify genes actively transcribed and differentially expressed in myeloid cells one month after repeated (3x) mTBI as compared to sham control mice. **b,** Heatmaps of candidate differentially expressed genes (DEGs) identified by RNA sequencing across brain regions. **c,** False discovery rate-adjusted p-values for candidate DEGs. **d,** Gene Ontology terms significantly associated with brainstem DEGs. Benjamini adjusted p-values. **e,** Imaging mass cytometry (IMC) workflow for detecting and phenotyping changes in brain tissue microenvironments after injury. **f,** T-SNE-based global phenotyping of single-cell image data. **g,** Phenograph analysis with unbiased identification of disease associated microglia (DAMs) (cluster 26, red box; CCR2^{-}, Iba-1^{+}, CD68^{hi}, ApoE^{hi}). **h,** Neighborhood analysis identifying changes in the frequency of associations between DAMs (Phenograph cluster 26) and phenograph-defined tissue microenvironments.

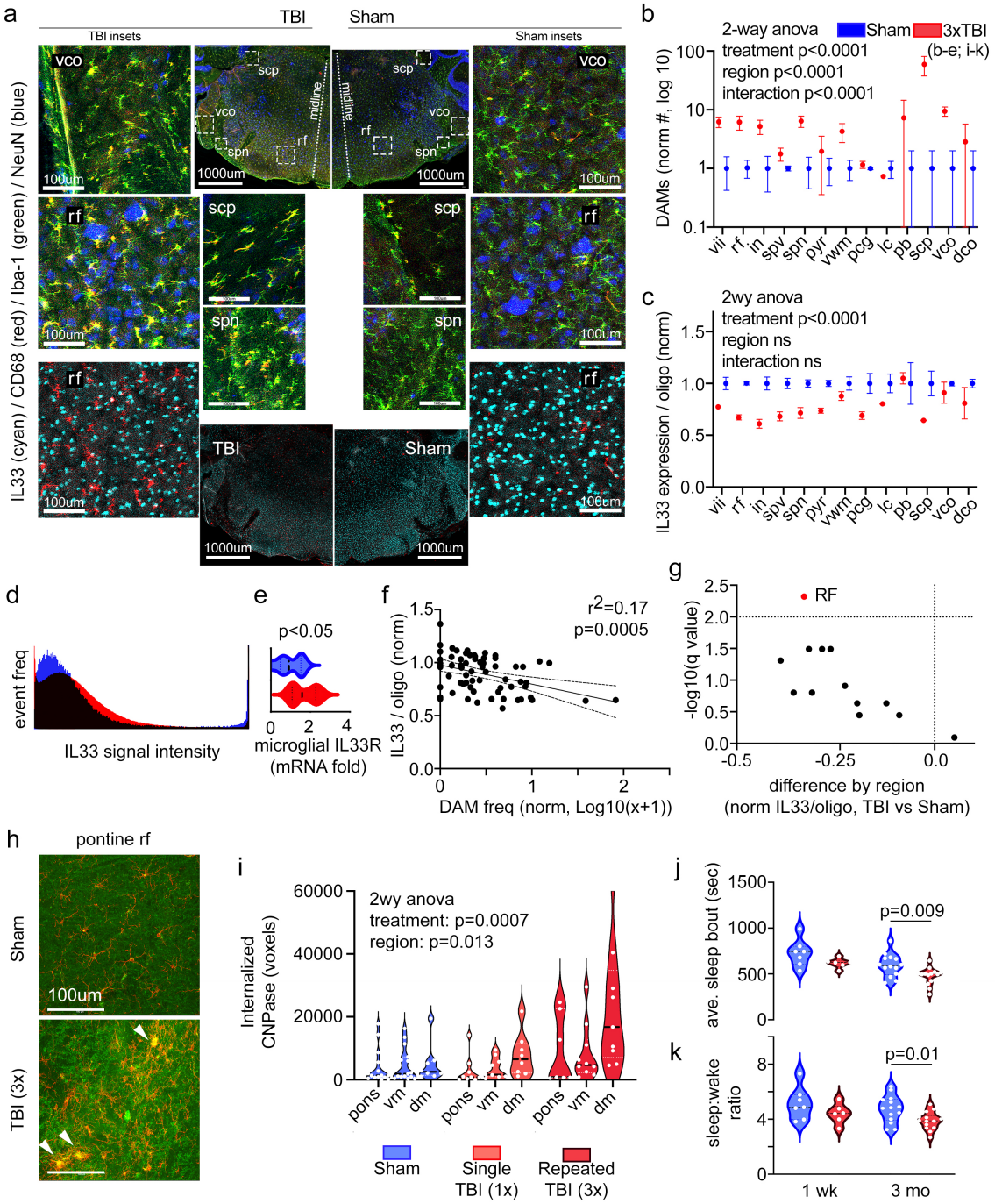

Figure 3. mTBI-induced IL33 release by oligodendrocytes is associated with microglial-mediated myelin remodeling. a, Representative IMC images of pontine hemisections from repeated TBI and sham mice. **b,** Average frequency of DAM per subject detected in IMC across pontine regions. **c,** Average expression of oligodendrocyte IL33 per mouse measured across pontine regions. **d,** Redistribution of nuclear oligodendroglial IL33 into the surrounding parenchymal microenvironment measured as a frequency histogram of IL33 signal intensity across pixels from insets in (**a**). **e,** Quantitation of microglial-specific IL33R transcript determined from microglial RiboTag mice (N=7 sham, 8 TBI (3x)). **f,** Release of

oligodendroglial IL33 predicts the accumulation of DAMs. DAM frequency significantly increased with loss of oligodendroglial IL33 among all pontine regions. Linear regression model. **g,** Volcano plot of q values (FDR-adjusted p-values) identifying robust myelin injury in the pontine RF, as measured by IL33 depletion from oligodendrocytes. **h,** Example of maximum intensity projection images from 3D confocal micrographs of microglia (red, Iba1) and myelin CNPase (green). Arrowheads denote microglial nodules consuming myelin. **i,** Violin plots show the total amount of CNPase internalized by microglial cells in each 50μm x 632μm^2 3D confocal image. **j,** Length of average sleep bouts and (**k**) sleep-to-wake ratios at 1 week and 3 months after repeated TBI. Red represents TBI data; blue represents sham control data. Data are a distribution of measured means from individual mice. Regions in **(b,c,g)** correspond to map in **Fig. 2e**. dm, dorsal medulla; rf, pontine reticular formation; scp, superior cerebellar peduncle; spn, spinal trigeminal nerve tract; vco, ventral cochlear nucleus; vm, ventral medulla.

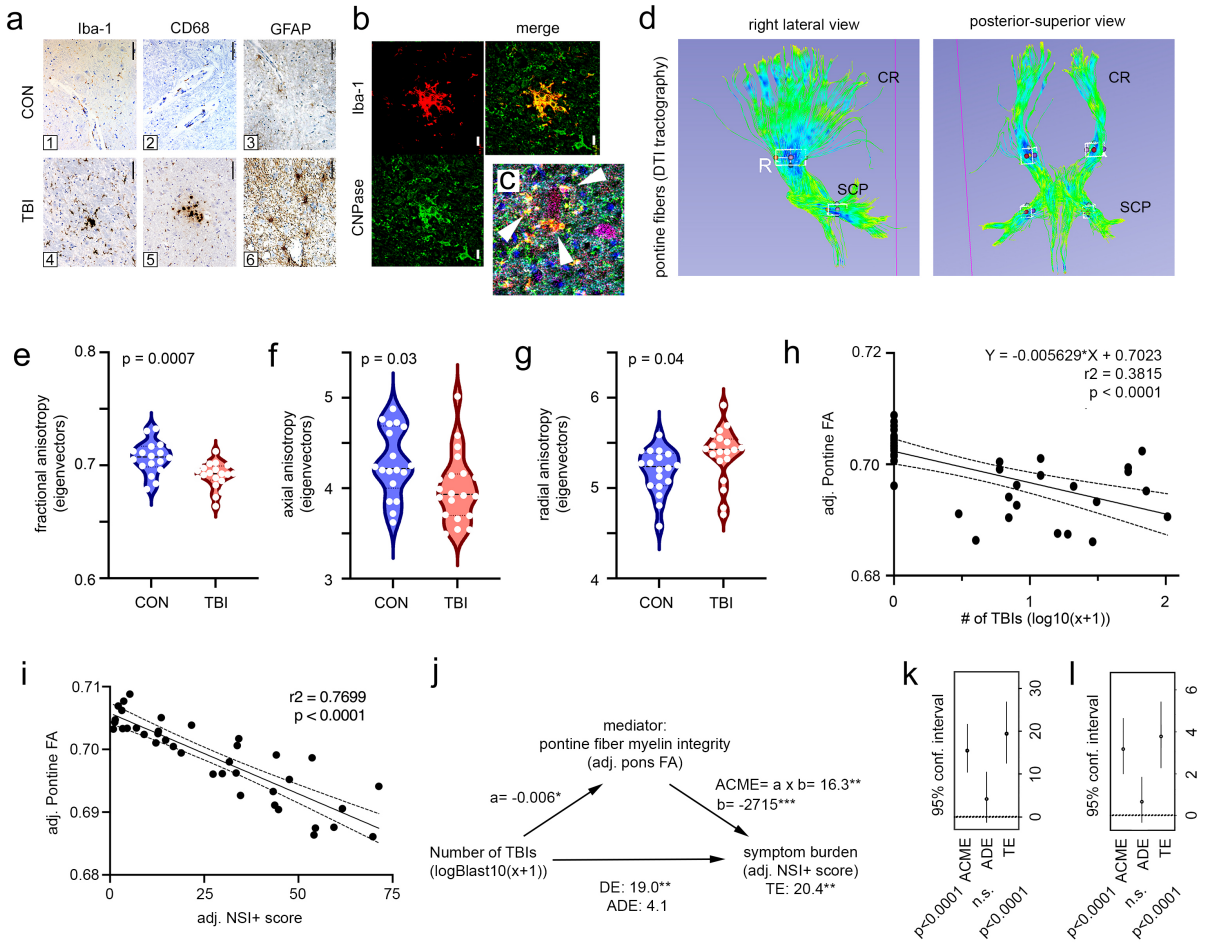

Figure 4. Pontine myelin injury mediates chronic blast-mTBI symptoms. a, Representative examples of brainstem glia in blast-mTBI and control subjects observed in three separate clinical neuropathology labs. **b,** Example confocal micrograph of clinical microglial nodule (red) with apparent internalization of myelin CNPase (green). **c,** IMC of pontine DAM (arrowheads) phagocytosing a neuron as seen in a clinical TBI subject. Purple, NeuN; cyan, CNPase; green, Iba-1; red, CD68; white, GFAP; blue, H3K27Me3. **d,** DTI tractography generated from pontine seed points. Boxes indicate the approximate locations of volumes of interest (VOIs) used for clinical DTI measures of major pontine projection tracts. Seed points were selected based on the acute pontine injury pattern observed in our animal study. CR, corona radiata; SCP, superior cerebellar peduncle. **e–h,** Quantification of chronic myelin injury is averaged across VOIs in living subjects. **e,** DTI fractional anisotropy (FA) is reduced in TBI subjects compared to control subjects; with groupwise changes in (**f**) axial and (**g**) radial anisotropy. **h,** Cumulative TBI-dose dependent decreases in pontine FA values adjusted for age and PTSD severity using linear regression modeling. **i,** Path diagram for causal mediation modelled with multivariable linear regression. ACME: adjusted causal mediation effect estimate, DE: direct effect estimate, ADE: adjusted direct effect estimate, TE total effect estimate. *p<0.05, **p<0.01, ***p<0.001. **j,** ACMEs for NSI+ total score related to blast-mTBI as mediated by reductions in mean pontine fiber FA (adjusted for age and PTSD). **k,** Results of bootstrap validation of mediation path illustrated in **(j)**. **l,** Boot-strap validated mediation analysis of blast-induced pontine fiber injury

to cause sleep injury using PTSD and age-adjusted PSQI total scores. Two-tailed t-tests in (**e**-**g**). Scale bars are (**e**) 100μm and (**b, i**) 10μm.

Supplemental Table 1.

Table S1. Table of candidate DEGs previously reported

	Ensembl gene number	Official Gene Symbol	Mouse Genome Informatics ID	UniProtKB	Previous Reports by PubMed ID
Candidates in Frontal Cortex	ENSMUSG00000027122.15	Arl14ep	MGI:1926020	Q8BIX3	
	ENSMUSG00000073102.7	Drc1	MGI:2685906	Q3USS3	
	ENSMUSG00000056116.18	H2-T22	MGI:95956	Q31615	
	ENSMUSG00000072294.5	Klf12	MGI:1333796	O35738	
	ENSMUSG00000090553.8	Snrpe	MGI:98346	P62305	
	ENSMUSG00000046985.11	Tapt1	MGI:2683537	Q4VBD2	
	ENSMUSG00000041353.12	Tmem29	MGI:1923420	A2ANF5	
	ENSMUSG00000041747.3	Utp15	MGI:2145443	Q8C7V3	
	ENSMUSG00000103567.1	Pcdhga5	MGI:1935217	Q91XY3	
Candidates in Cerebellum	ENSMUSG00000024998.17	Plce1	MGI:1921305	Q8K4S1	
	ENSMUSG00000064043.13	Trerf1	MGI:2442086	Q8BXJ2	
	ENSMUSG00000022382.15	Wnt7b	MGI:98962	P28047	
	ENSMUSG00000030697.7	Ppp4c	MGI:1891763	P97470	
	ENSMUSG00000056306.5	Sertm1	MGI:3607715	Q8CD78	
	ENSMUSG00000037761.16	Actr5	MGI:1924748	Q80US4	
	ENSMUSG00000033021.16	Gmppa	MGI:1916330	Q922H4	
	ENSMUSG00000021884.18	Hacl1	MGI:1929657	Q9QXE0	
	ENSMUSG00000032360.16	Hcrtr2	MGI:2680765	P58308	
	ENSMUSG00000046523.5	Kctd4	MGI:1914766	Q9D7X1	
	ENSMUSG00000030226.12	Lmo3	MGI:102810	Q8BZL8	
	ENSMUSG00000024146.9	Cript	MGI:1929655	O70333	
	ENSMUSG00000052928.8	Ctif	MGI:2685518	Q6PEE2	
	ENSMUSG00000048644.8	Ctxn1	MGI:88566	Q8K129	
Candidates in Brainstem	ENSMUSG00000011148.14	Adssl1	MGI:87947	P28650	
	ENSMUSG00000021557.15	Agtpbp1	MGI:2159437	Q641K1	
	ENSMUSG00000025135.12	Anapc11	MGI:1913406	Q9CPX9	
	ENSMUSG00000002985.16	Apoe	MGI:88057	P08226	30082275, 33333014, 30471926, 30185219, 31998844, scrnaseq: 33257666, 28602351, 30206190, 32371549, 31768052, 31061494, mass cytometry: 31740814, 32811567
	ENSMUSG00000076441.9	Ass1	MGI:88090	P16460	11406294, 17900569, 11556547
	ENSMUSG00000038539.15	Atf5	MGI:2141857	O70191	
	ENSMUSG00000019943.10	Atp2b1	MGI:104653	G5E829	
	ENSMUSG00000022956.11	Atp5o	MGI:106341	Q9DB20	
	ENSMUSG00000006273.14	Atp6v1b2	MGI:109618	P62814	
	ENSMUSG00000002602.16	Axl	MGI:1347244	Q00993	30471926, 30185219, scrnaseq: 33257666, 28602351, 30206190, 31061494, 33029008
	ENSMUSG00000043300.2	B3galnt1	MGI:1349405	Q920V1	
	ENSMUSG00000051223.14	Bzw1	MGI:1914132	Q9CQC6	
	ENSMUSG00000056737.14	Capg	MGI:1098259	P24452	30082275
	ENSMUSG00000019122.8	Ccl9	MGI:104533	P51670	32059938
	ENSMUSG00000034652.12	Cd300a	MGI:2443411	Q6SJQ0	
	ENSMUSG00000000682.7	Cd52	MGI:1346088	Q64389	ribotag: 30082275, scrnaseq 30471926, 30185219, 31998844, 30206190
	ENSMUSG00000018774.13	Cd68	MGI:88342	P31996	26764157, ribotag: 33333014, nanostring: 31440141, 33452227, scrnaseq: 33257666, 30206190, 31061494, 33029008, masscytometry: 31740814, 32470397, 32917850, 32917850
	ENSMUSG00000015396.4	Cd83	MGI:1328316	O88324	31440141, scrnaseq: 33257666
	ENSMUSG00000046722.14	Cdc42se1	MGI:1889510	Q8BHL7	
	ENSMUSG00000050370.4	Ch25h	MGI:1333869	Q9Z0F5	ribotag: 29777220, scrnaseq: 31998844, 32371549
	ENSMUSG00000068129.5	Cst7	MGI:1298217	O89098	30082275, 30471926, 31998844, scrnaseq: 33257666, 28602351, 30206190, 31061494
	ENSMUSG00000021939.8	Ctsb	MGI:88561	P10605	30185219, 31998844, scrnaseq: 33257666, 28602351, 30206190, 32371549, 31061494, 33029008
	ENSMUSG00000037149.10	Ddx1	MGI:2144727	Q91VR5	
	ENSMUSG00000063904.3	Dpp3	MGI:1922471	Q99KK7	
	ENSMUSG00000022842.18	Ece2	MGI:1101356	B2RQR8	19541930
	ENSMUSG00000038418.7	Egr1	MGI:95295	P08046	31998844, scrnaseq: 32371549, 31061494
	ENSMUSG00000058655.9	Eif4b	MGI:95304	Q8BGD9	
	ENSMUSG00000074802.11	Gas2l3	MGI:1918780	Q3UWW6	
	ENSMUSG00000072772.3	Grcc10	MGI:1315201	O35127	
	ENSMUSG00000020330.16	Hmmr	MGI:104667	Q00547	
	ENSMUSG00000050335.17	Lgals3	MGI:96778	P16110	30082275, 30471926, 31998844, scrnaseq: 33257666, 29020624, 31061494
	ENSMUSG00000015568.16	Lpl	MGI:96820	P11152	30082275, 30471926, 31998844, scrnaseq: 33257666, 28602351, 30206190
	ENSMUSG00000034854.8	Mfsd12	MGI:3604804	Q3U481	
	ENSMUSG00000033307.7	Mif	MGI:96982	P34884	scrnaseq 30471926 (development), 31998844, 33029008
	ENSMUSG00000022453.8	Naga	MGI:1261422	Q9QWR8	
	ENSMUSG00000027698.14	Nceh1	MGI:2443191	Q8BLF1	
	ENSMUSG00000041560.12	Nop53	MGI:2154441	Q8BK35	
	ENSMUSG00000040771.14	Oard1	MGI:2146818	Q8R5F3	
	ENSMUSG00000023191.9	P3h3	MGI:1315208	Q8CG70	
	ENSMUSG00000046139.7	Patl1	MGI:2147679	Q3TC46	
	ENSMUSG00000031921.17	Terf2	MGI:1195972	O35144	
	ENSMUSG00000027750.16	Postn	MGI:1926321	Q62009	25580734 (in glioma, recruits macs)
	ENSMUSG00000022951.16	Rcan1	MGI:1890564	Q9JHG6	20967884, 23144708, 18485347,
	ENSMUSG00000032518.6	Rpsa	MGI:105381	P14206	19196078
	ENSMUSG00000039153.16	Runx2	MGI:99829	Q08775	24768841 runx2 driven by P2X7 activity
	ENSMUSG00000024737.2	Slc15a3	MGI:1929691	Q8BPX9	
	ENSMUSG00000069793.12	Slfn9	MGI:2445121	B1ARD6	
	ENSMUSG00000029304.14	Spp1	MGI:98389	P10923	30082275, 31998844, 28101531, 31088570, 15804504, 12132583, scrnaseq: 28602351, 33029008
	ENSMUSG00000029538.14	Srsf9	MGI:104896	Q9D0B0	
	ENSMUSG00000031995.9	St14	MGI:1338881	P56677	30082275
	ENSMUSG00000022415.12	Syngr1	MGI:1328323	O55100	scrnaseq of ALS mouse brainstem: 32360664
	ENSMUSG00000037108.13	Zcwpw1	MGI:2685899	Q6IR42	26919393 (AD risk polymorhism associated with microglial expression)
	ENSMUSG00000027506.15	Tpd52	MGI:107749	Q62393	
	ENSMUSG00000056019.12	Zfp709	MGI:2384299	Q99PJ6	

Supplemental Table 2.

Table S2. Table of imaging mass cytometry antibodies

Mass Channel	Antibody	Supplier	Suppler Cat #	LOT #	[ug/ml] (final)	Validation
141	mouse monoclonal anti- human Smooth muscle Actin (Clone 1A4)	FLUIDIGM	3141017D	1261907	2	endogenous expression in Human, rat, mouse; KO validated for IHC / IF / WB
142	rabbit monoclonal anti- human APP y188	Abcam	ab256586	GR3337706-2	6.5	endogenous expression in Human, rat, mouse; KO validated for IHC / IF / WB
143	rabbit monoclonal anti- human AQP4 (Clone D1F8E)	Cell Signaling Technologies	59678BF	2	8	endogenous expression in Human, rat, mouse; validated by IHC / IF / WB / IP
144	rabbit monoclonal anti- mouse calbindin (Clone EPR22698-236)	Abcam	ab255691	GR3279332-2	3	endogenous expression in rat, mouse; validated by IHC / IF / WB / IP
145	rabbit monoclonal anti- mouse CD63 (Clone EPR21151)	Abcam	ab227892	GR3274484-1	8	endogenous expression in mouse; validated by IF / WB
147	rabbit monoclonal anti-CD31 (Clone D8V9E)	Cell Signaling Technologies	92841BF	3	1.6	endogenous expression, with positive and negative controls
148	mouse monoclonal anti- human pan cytokeratin (C11)	FLUIDIGM	3148020D	1681901	2.5	endogenous expression in rat, mouse; validated by IHC / IF
149	rabbit monoclonal anti- h3k27me3 (Clone C36B11)	Cell Signaling Technologies	9733BF	20	5	endogenous expression in rat, mouse, human; validated by IHC / IF / WB / IP
150	rat monoclonal anti- mouse CD3 (Clone 17A2)	Biolegend	100238	B305614	10	endogenous expression for mouse, reported applications FC, ICFC, ICC, IHC, IP, WB, FA
151	rabbit monoclonal anti- thrombospondin (Clone EPR22928-10)	Abcam	ab263952	GR3297011-2	6.5	endogenous expression in rat, mouse, human; validated by IHC / IF / WB / IP
152	rabbit monoclonal anti- htt (Clone EPR5526)	Abcam	ab209668	GR3271602-1	3.3	endogenous expression in human, rat, mouse; KO validated, for IHC / IF / WB / Flow Cyt
153	rat monoclonal anti- mouse CD8a (Clone 53-6.7)	FLUIDIGM	clone 53-6.7	101806	6.5	endogenous expression in mouse; validated, for IF / Flow Cyt
154	rabbit monoclonal anti- mouse CCR2 (Clone EPR20844-15)	Abcam	ab273061	GR3341831-1	12.5	endogenous expression in mouse, rat; validated, for IF / IP / IHC / Flow Cyt
155	rabbit monoclonal anti- ApoE (Clone EPR3326)	Abcam	ab215274	GR3309685-1	5	endogenous expression in Human, rat, mouse; KO validated for IP/ WB
156	rabbit monoclonal anti- mouse iNOS (Clone D6B6S)	Cell Signaling Technologies	13120BF	6	10	endogenous expression in mouse; validated for IP/ WB / IF / Flow Cyt
158	goat polyclonal anti- mouse IL33	R&D	AF3626	YJE0819121	3.3	endogenous expression in mouse; validated for ELISA / IP / Flow Cyt / IF / IHC
159	rabbit monoclonal anti- human PSD95 (Clone D74D3)	Cell Signaling Technologies	3409BF	5	4	endogenous expression in mouse, rat, human; validated for IHC / WB.
160	mouse monoclonal anti- human CD184 (Clone 12G5)	Biolegend	306523	B235925	8	endogenous expression in human; validated for Flow Cyt / IF / IHC. Used as negative control in mouse.
161	rabbit monoclonal anti- fibrinogen (Clone EPR18145-84)	Abcam	ab227063	GR3194483-1	10	endogenous expression in mouse, rat, human; validated for Flow Cyt / IHC.
162	rabbit monoclonal anti- human Tau (Clone D1M9X)	Cell Signaling Technologies	29384	2	3.3	endogenous expression in mouse, rat, human; KO validated for Flow Cyt / IHC / WB / IF.
163	rabbit monoclonal anti- EAAT2 (Clone EPR19798)	Abcam	271970	GR3340947-1	8	endogenous expression in mouse, rat, human; validated for IHC / WB / IP.
164	rabbit monoclonal anti- mouse CD68 (Clone E3O7V)	Cell Signaling Technologies	97778BF	2	8	endogenous expression in mouse; positive and negative control validated for IHC / IF / WB / Flow Cyt.
165	mouse monoclonal anti- mouse/rat MAP2 (Clone SMI 52)	Biolegend	801801	B266835	5	endogenous expression in mouse, rat; positive and negative control validated for ELISA / IHC / IF / WB / Flow Cyt.
166	rabbit monoclonal anti- beta-2 Microglobulin (Clone EPR21752-214)	Abcam	ab237032	GR3234347-2	7.5	endogenous expression in mouse, rat, human; KO validated for IHC / IP / WB / Flow Cyt.
167	rabbit monoclonal anti- Vascular Amyloid (Clone mOC31)	Abcam	ab251334	GR3336463-1	3	endogenous expression in mouse, human; validated for IHC .
168	mouse monoclonal anti- Ki67 (Clone B56)	FLUIDIGM	3168022D	2411806	2.5	endogenous expression in mouse, rat, human; KO validated for IF / IHC / Flow Cyt.
169	hamster monoclonal anti- mouse MCP1 (Clone 2H5)	Biolegend	505912	B296185	10	endogenous expression in mouse, rat, human; validated for WB / IHC / Flow Cyt / ELISA.
170	rabbit monoclonal anti- dopamine beta hydroxylase	Abcam	ab223130	GR3180359-1	4	endogenous expression in mouse, rat, human; validated for WB / IHC / IP.
171	rat monoclonal anti- mouse/human CD44 (Clone IM7)	Biolegend	103046	B338510		endogenous expression in mouse, human; validated for IHC / IP / IF.
172	rabbit polyclonal anti- human LINGO1	Sino Biological	101252-T08	HD10MA1826-B	3.5	endogenous expression in mouse, human; validated for IHC.
173	mouse monoclonal anti- gfap (Clone SMI 22)	Biolegend	835304	missing	0.8	endogenous expression in mouse, rat, human; validated for IHC / ICC / WB.
174	rabbit monoclonal anti- Iba (Clone EPR16589)	Abcam	ab221790	GR3347998-4	1.6	endogenous expression in mouse, rat, human; validated for IHC / ICC / WB.
175	rabbit monoclonal anti- NeuN (Clone EPR12763)	Abcam	ab209898	GR3271481-4	10	endogenous expression in mouse, rat, human; validated for IHC / ICC / IF / WB / Flow Cyt.
176	mouse monoclonal anti- CNPase (Clone SMI-91)	Biolegend	836404	missing	2.5	endogenous expression in mouse, rat, human; validated for IHC / ICC / IF / WB.
195	PM1	FLUIDIGM	TIS-00001 (ICSK1)	1742007	4	
196	PM2	FLUIDIGM	TIS-00001 (ICSK2)	1742008	4	endogenous expression in mouse, human; validated for IHC.
198	PM3	FLUIDIGM	TIS-00001 (ICSK3)	1882005	4	

905 Supplemental Table 3.
906
907 Subject Demographics

Demographics	Mean (SD), range
Age (years)	31.5 (9.4), 23–60
Education (years)	13.7 (1.5), 11–16
Race, nonwhite, *n* (%)	8 (24.2%)
APOE-ε4–positive (%)	8 (25.8%)
Blast exposures	
Number of blast-related mild TBIs during military service (lifetime)	25.8 (24.2), 1–102, Median = 13
Number of lifetime mild TBIs with loss of consciousness	1.8 (1.8), 0–6, Median = 1
Time since last blast-related mild TBI (years)	3.6 (1.5), 1–7, Median = 4
Behavioral and neurological measures	
PCL-M score	40 (19.7), 17–79, Median = 34
PHQ-9 score	9.6 (7.4), 0–25
PSQI score	8.6 (5.8), 1–20;
AUDIT-C score	3.4 (2.7), 0–9
NSI total score	20.6 (17.8), 0–59, Median = 18
NSI+ total score	25.4 (21.7), 0-73, Median = 22

908

909 Supplemental Figure 1.
910

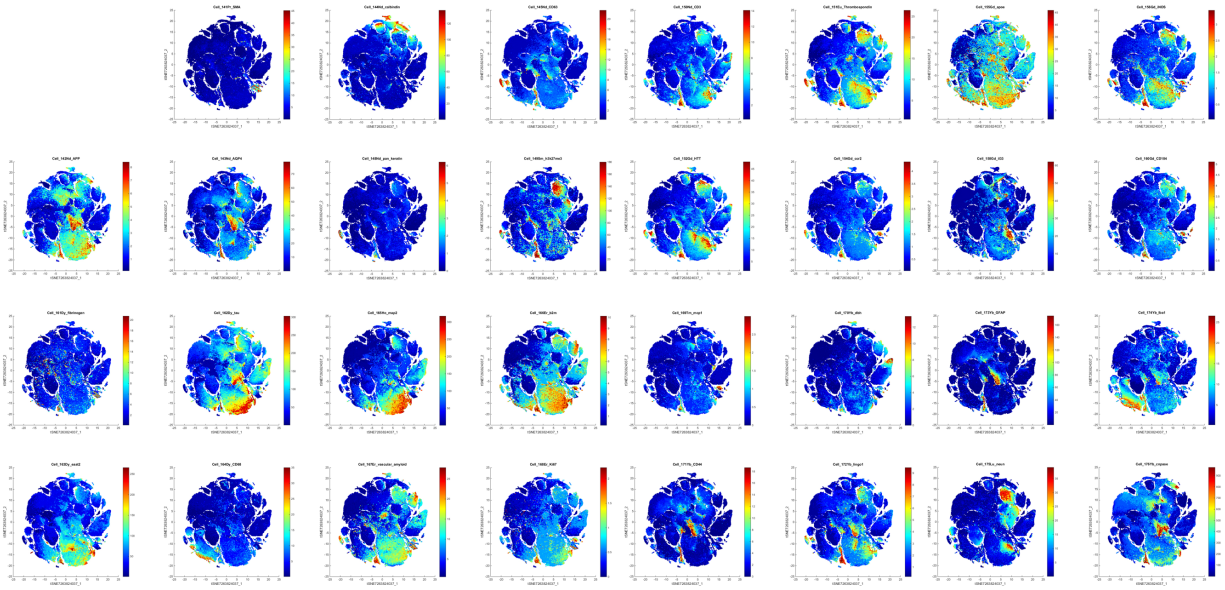

911
912
913 **Figure S1. T-SNE plots for separate IMC mass channels included in the study.**
914
915

916 Supplemental Figure 2.
917
918

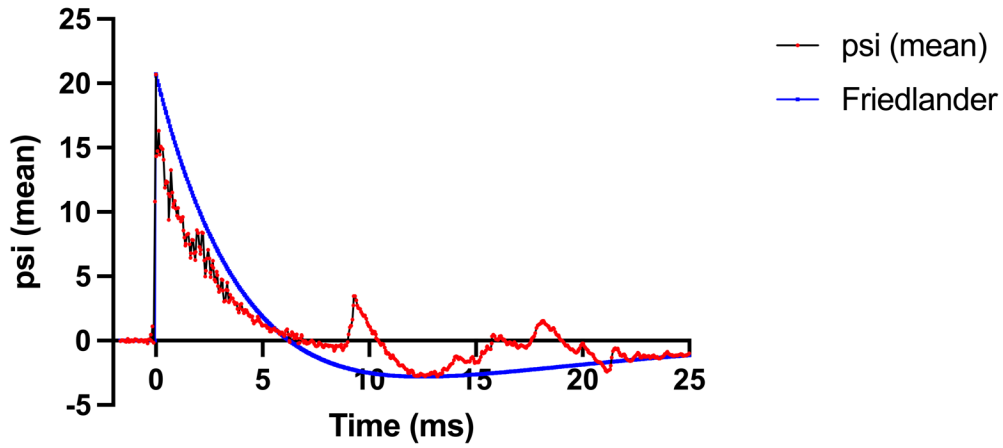

919
920
921 **Figure S2. Average overpressure waveform for diffuse mTBI model.** Data represent the
922 average timestamped pressure measurements taken 5 cm above the animal over 102 trials
923 occurring over several days (red shown with black bars indicating ±SEM). The blue line
924 represents the idealized Friedlander waveform produced by 11.35 kg of trinitrotoluene (TNT) at
925 a distance of 6.2 m.
926

927 Supplemental Figure 3.
928

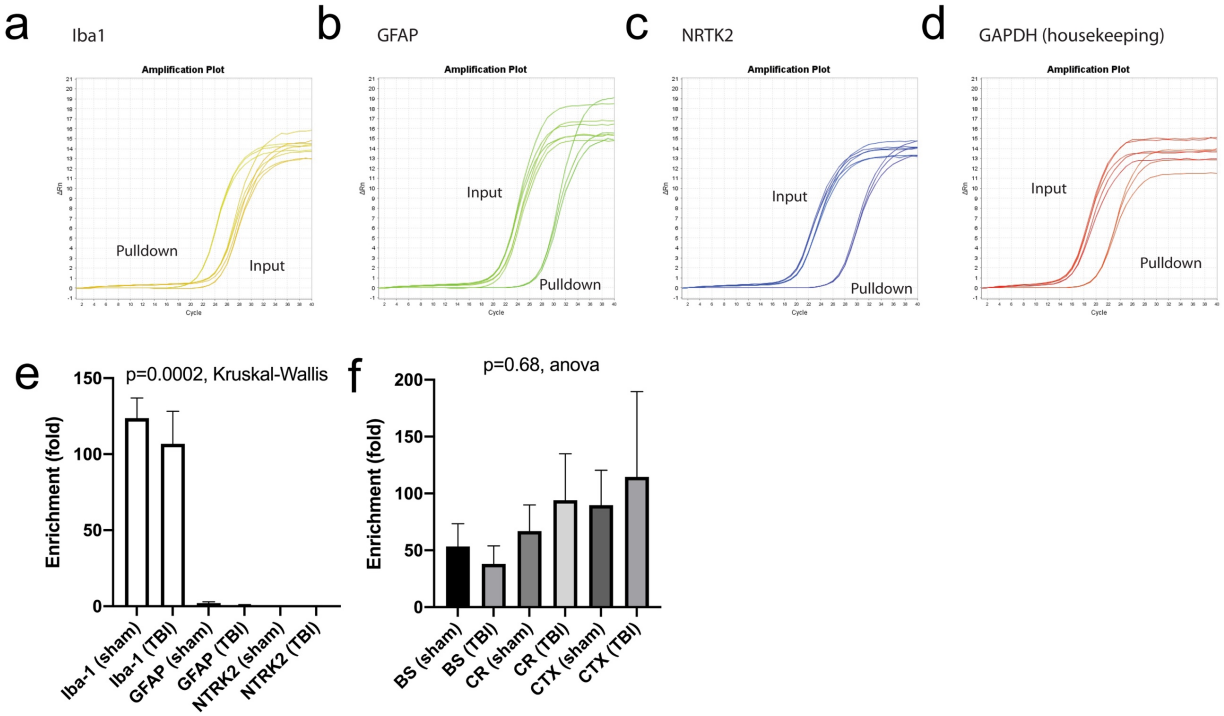

929
930
931
932 **Figure S3. Analysis of mRNA enrichment by RiboTag immunoprecipitation. (a-d)** Real-
933 time (RT) PCR amplification curves of **(a)** microglial Iba-1, **(b)** astrocytic GFAP, **(c)** neuronal
934 NTRK2, and **(d)** the ubiquitous housekeeping gene GAPDH. Each curve represents either
935 immunoprecipitated mRNA or input samples from individual mice. **(e)** Quantification of RT-
936 PCR enrichment analyses using cortical hemisection tissue (N=4-8 per tissue). **(f)** Relative Iba-1
937 enrichment across brainstem (BS), cerebellum (CR), and cortical tissues (CTX) (N=2-6 per
938 tissue).
939

940 Supplemental Figure 4.
941

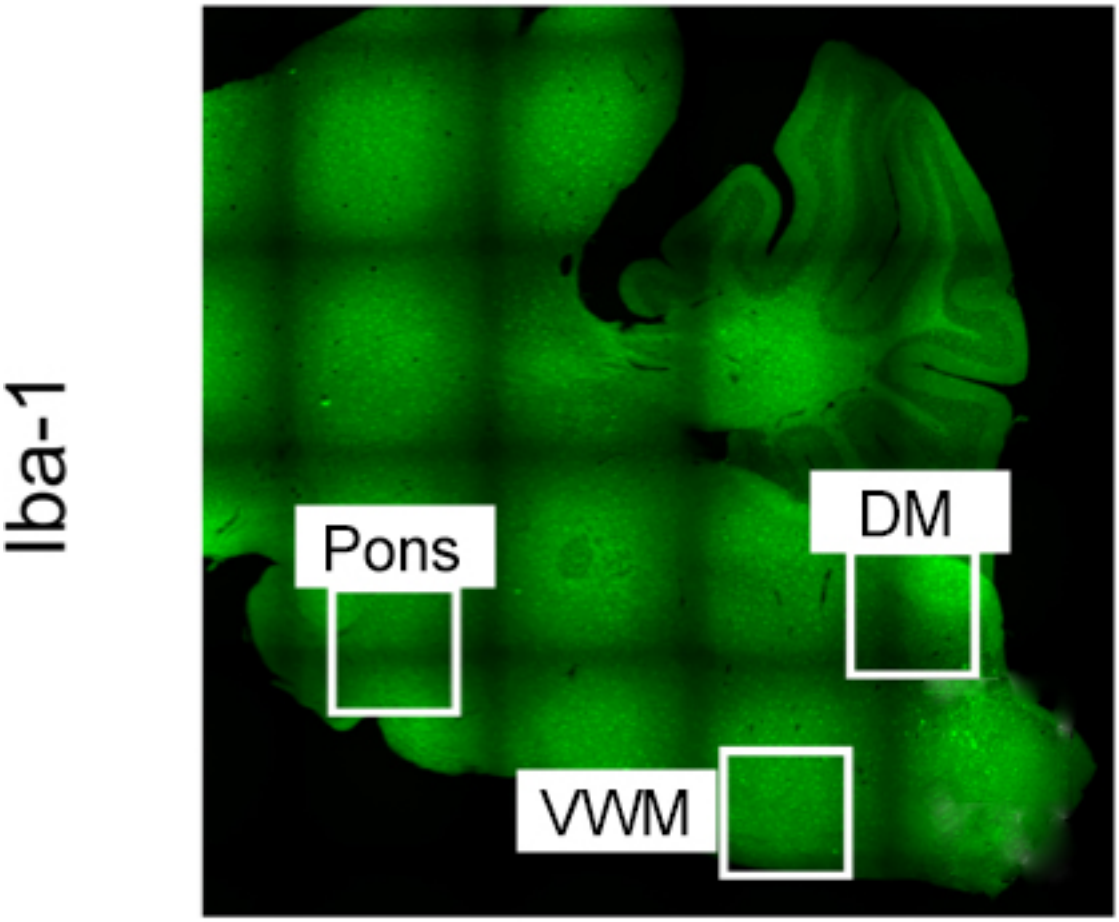

942
943 **Figure S4. Locations used for confocal microscopy analyses of microglia internalization of**
944 **myelin CNPase.** Sagittal mouse brain section shows location of images taken from brainstem
945 pons, dorsal medulla (DM), and ventral white matter (VWM).
946

Supplemental Figure 5

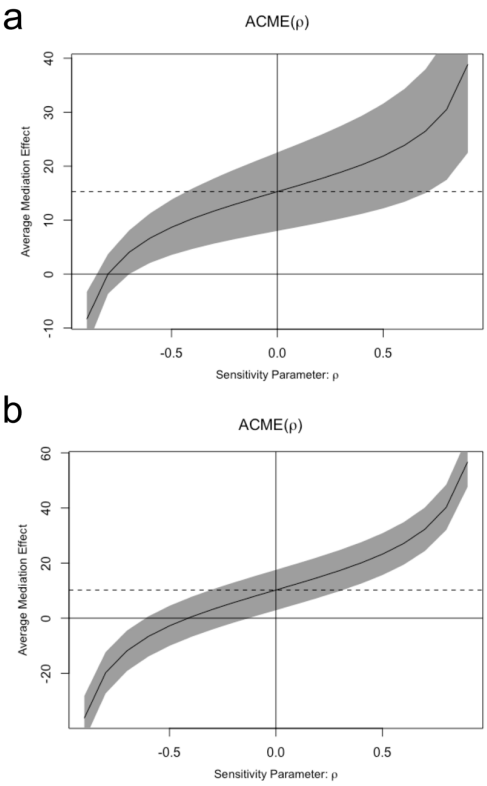

Figure S5. Sensitivity analyses for Pons FA mediation of cumulative blast exposure effects. **a)** Sensitivity analysis for mediated effects on TBI-associated neurobehavioral symptoms using NSI+ total score. The results show that for the point estimate of the to be zero, the correlation of ACME between the adjusted Pons FA value and PSQI total score must be approximately -0.9. b) Sensitivity analysis for mediated effects on sleep using PSQI total score. The results show that for the point estimate of the to be zero, the correlation of ACME between the adjusted Pons FA value and PSQI total score must be approximately -0.4. Gray area is the 95% CI.

961 References
962
963 1. Dewan, M.C., *et al.* Estimating the global incidence of traumatic brain injury. *J*
964 *Neurosurg*, 1-18 (2018).
965 2. Renga, V. Clinical Evaluation and Treatment of Patients with Postconcussion Syndrome.
966 *Neurol Res Int* **2021**, 5567695 (2021).
967 3. Benusa, S.D. & Lafrenaye, A.D. Microglial process convergence on axonal segments in
968 health and disease. *Neuroimmunol Neuroinflamm* **7**, 23-39 (2020).
969 4. Eyolfson, E., Khan, A., Mychasiuk, R. & Lohman, A.W. Microglia dynamics in
970 adolescent traumatic brain injury. *J Neuroinflammation* **17**, 326 (2020).
971 5. Meaney, D.F., *et al.* Biomechanical analysis of experimental diffuse axonal injury. *J*
972 *Neurotrauma* **12**, 689-694 (1995).
973 6. Lippa, S.M., Pastorek, N.J., Benge, J.F. & Thornton, G.M. Postconcussive symptoms
974 after blast and nonblast-related mild traumatic brain injuries in Afghanistan and Iraq war
975 veterans. *J Int Neuropsychol Soc* **16**, 856-866 (2010).
976 7. Mac Donald, C.L., *et al.* Prospectively assessed clinical outcomes in concussive blast vs
977 nonblast traumatic brain injury among evacuated US military personnel. *JAMA Neurol*
978 **71**, 994-1002 (2014).
979 8. Cooper, D.B., Vanderploeg, R.D., Armistead-Jehle, P., Lewis, J.D. & Bowles, A.O.
980 Factors associated with neurocognitive performance in OIF/OEF servicemembers with
981 postconcussive complaints in postdeployment clinical settings. *J Rehabil Res Dev* **51**,
982 1023-1034 (2014).
983 9. Belanger, H.G., *et al.* Symptom complaints following reports of blast versus non-blast
984 mild TBI: does mechanism of injury matter? *Clin Neuropsychol* **25**, 702-715 (2011).
985 10. Cooper, D.B., *et al.* Association between combat stress and post-concussive symptom
986 reporting in OEF/OIF service members with mild traumatic brain injuries. *Brain Inj* **25**,
987 1-7 (2011).
988 11. Belanger, H.G., Kretzmer, T., Yoash-Gantz, R., Pickett, T. & Tupler, L.A. Cognitive
989 sequelae of blast-related versus other mechanisms of brain trauma. *J Int Neuropsychol*
990 *Soc* **15**, 1-8 (2009).
991 12. Huber, B.R., *et al.* Blast exposure causes early and persistent aberrant phospho- and
992 cleaved-tau expression in a murine model of mild blast-induced traumatic brain injury. *J*
993 *Alzheimers Dis* **37**, 309-323 (2013).
994 13. McKee, A.C., Daneshvar, D.H., Alvarez, V.E. & Stein, T.D. The neuropathology of
995 sport. *Acta Neuropathol* **127**, 29-51 (2014).
996 14. Oppenheimer, D.R. Microscopic lesions in the brain following head injury. *J Neurol*
997 *Neurosurg Psychiatry* **31**, 299-306 (1968).
998 15. Korn, A., Golan, H., Melamed, I., Pascual-Marqui, R. & Friedman, A. Focal cortical
999 dysfunction and blood-brain barrier disruption in patients with Postconcussion syndrome.
1000 *J Clin Neurophysiol* **22**, 1-9 (2005).
1001 16. Logsdon, A.F., *et al.* Blast exposure elicits blood-brain barrier disruption and repair
1002 mediated by tight junction integrity and nitric oxide dependent processes. *Sci Rep* **8**,
1003 11344 (2018).
1004 17. Meabon, J.S., *et al.* Repetitive blast exposure in mice and combat veterans causes
1005 persistent cerebellar dysfunction. *Sci Transl Med* **8**, 321ra326 (2016).

18. Corsellis, J.A., Bruton, C.J. & Freeman-Browne, D. The aftermath of boxing. *Psychol Med* **3**, 270-303 (1973).
19. Unterberg, A.W., Stover, J., Kress, B. & Kiening, K.L. Edema and brain trauma. *Neuroscience* **129**, 1021-1029 (2004).
20. Kang, J.H. & Lin, H.C. Increased risk of multiple sclerosis after traumatic brain injury: a nationwide population-based study. *J Neurotrauma* **29**, 90-95 (2012).
21. Lehman, E.J., Hein, M.J., Baron, S.L. & Gersic, C.M. Neurodegenerative causes of death among retired National Football League players. *Neurology* **79**, 1970-1974 (2012).
22. Gardner, R.C.*, et al.* Mild TBI and risk of Parkinson disease: A Chronic Effects of Neurotrauma Consortium Study. *Neurology* **90**, e1771-e1779 (2018).
23. Keren-Shaul, H.*, et al.* A Unique Microglia Type Associated with Restricting Development of Alzheimer's Disease. *Cell* **169**, 1276-1290 e1217 (2017).
24. Haimon, Z.*, et al.* Re-evaluating microglia expression profiles using RiboTag and cell isolation strategies. *Nat Immunol* **19**, 636-644 (2018).
25. Mattei, D.*, et al.* Enzymatic Dissociation Induces Transcriptional and Proteotype Bias in Brain Cell Populations. *Int J Mol Sci* **21**(2020).
26. Olah, M.*, et al.* Single cell RNA sequencing of human microglia uncovers a subset associated with Alzheimer's disease. *Nat Commun* **11**, 6129 (2020).
27. Xu, J.*, et al.* Multimodal single-cell/nucleus RNA sequencing data analysis uncovers molecular networks between disease-associated microglia and astrocytes with implications for drug repurposing in Alzheimer's disease. *Genome Res* **31**, 1900-1912 (2021).
28. Fu, R., Shen, Q., Xu, P., Luo, J.J. & Tang, Y. Phagocytosis of microglia in the central nervous system diseases. *Mol Neurobiol* **49**, 1422-1434 (2014).
29. Trapp, B.D. & Nave, K.A. Multiple sclerosis: an immune or neurodegenerative disorder? *Annu Rev Neurosci* **31**, 247-269 (2008).
30. Rasband, M.N.*, et al.* CNP is required for maintenance of axon-glia interactions at nodes of Ranvier in the CNS. *Glia* **50**, 86-90 (2005).
31. Singh, S.*, et al.* Microglial nodules in early multiple sclerosis white matter are associated with degenerating axons. *Acta Neuropathol* **125**, 595-608 (2013).
32. Viola-Saltzman, M. & Watson, N.F. Traumatic brain injury and sleep disorders. *Neurol Clin* **30**, 1299-1312 (2012).
33. Mathias, J.L. & Alvaro, P.K. Prevalence of sleep disturbances, disorders, and problems following traumatic brain injury: a meta-analysis. *Sleep Med* **13**, 898-905 (2012).
34. Ouellet, M.C., Beaulieu-Bonneau, S. & Morin, C.M. Insomnia in patients with traumatic brain injury: frequency, characteristics, and risk factors. *J Head Trauma Rehabil* **21**, 199-212 (2006).
35. Collen, J., Orr, N., Lettieri, C.J., Carter, K. & Holley, A.B. Sleep disturbances among soldiers with combat-related traumatic brain injury. *Chest* **142**, 622-630 (2012).
36. Clinchot, D.M., Bogner, J., Mysiw, W.J., Fugate, L. & Corrigan, J. Defining sleep disturbance after brain injury. *Am J Phys Med Rehabil* **77**, 291-295 (1998).
37. Donohue, K.D., Medonza, D.C., Crane, E.R. & O'Hara, B.F. Assessment of a non-invasive high-throughput classifier for behaviours associated with sleep and wake in mice. *Biomed Eng Online* **7**, 14 (2008).
38. Flores, A.E.*, et al.* Pattern recognition of sleep in rodents using piezoelectric signals generated by gross body movements. *IEEE Trans Biomed Eng* **54**, 225-233 (2007).

39. Rowe, R.K., *et al.* Diffuse brain injury induces acute post-traumatic sleep. *PLoS One* **9**, e82507 (2014).
40. Liu, H., *et al.* Aging of cerebral white matter. *Ageing Res Rev* **34**, 64-76 (2017).
41. Farrell-Carnahan, L., Franke, L., Graham, C. & McNamee, S. Subjective sleep disturbance in veterans receiving care in the Veterans Affairs Polytrauma System following blast-related mild traumatic brain injury. *Mil Med* **178**, 951-956 (2013).
42. Norris, J.N., Sams, R., Lundblad, P., Frantz, E. & Harris, E. Blast-related mild traumatic brain injury in the acute phase: acute stress reactions partially mediate the relationship between loss of consciousness and symptoms. *Brain Inj* **28**, 1052-1062 (2014).
43. Leng, Y., *et al.* Traumatic Brain Injury and Incidence Risk of Sleep Disorders in Nearly 200,000 US Veterans. *Neurology* **96**, e1792-e1799 (2021).
44. Meythaler, J.M., Peduzzi, J.D., Eleftheriou, E. & Novack, T.A. Current concepts: diffuse axonal injury-associated traumatic brain injury. *Arch Phys Med Rehabil* **82**, 1461-1471 (2001).
45. van Horssen, J., *et al.* Clusters of activated microglia in normal-appearing white matter show signs of innate immune activation. *J Neuroinflammation* **9**, 156 (2012).
46. Aoun, R., Rawal, H., Attarian, H. & Sahni, A. Impact of traumatic brain injury on sleep: an overview. *Nat Sci Sleep* **11**, 131-140 (2019).
47. Nassan, M. & Videnovic, A. Circadian rhythms in neurodegenerative disorders. *Nat Rev Neurol* **18**, 7-24 (2022).
48. Schiff, N.D. Central thalamic contributions to arousal regulation and neurological disorders of consciousness. *Ann N Y Acad Sci* **1129**, 105-118 (2008).
49. Edlow, B.L., *et al.* Neuroanatomic connectivity of the human ascending arousal system critical to consciousness and its disorders. *J Neuropathol Exp Neurol* **71**, 531-546 (2012).
50. Schiff, N.D. Recovery of consciousness after brain injury: a mesocircuit hypothesis. *Trends Neurosci* **33**, 1-9 (2010).
51. Steriade, M. Arousal: revisiting the reticular activating system. *Science* **272**, 225-226 (1996).
52. Moruzzi, G. & Magoun, H.W. Brain stem reticular formation and activation of the EEG. *Electroencephalogr Clin Neurophysiol* **1**, 455-473 (1949).
53. Newman, D.B. & Ginsberg, C.Y. Brainstem reticular nuclei that project to the cerebellum in rats: a retrograde tracer study. *Brain Behav Evol* **39**, 24-68 (1992).
54. Ryan, N.P., *et al.* White matter microstructure predicts longitudinal social cognitive outcomes after paediatric traumatic brain injury: a diffusion tensor imaging study. *Psychol Med* **48**, 679-691 (2018).
55. Drijkoningen, D., *et al.* Regional volumes in brain stem and cerebellum are associated with postural impairments in young brain-injured patients. *Hum Brain Mapp* **36**, 4897-4909 (2015).
56. De Andrés, I. & Reinoso-Suàrez, F. Participation of the cerebellum in the regulation of the sleep-wakefulness cycle through the superior cerebellar peduncle. *Arch Ital Biol* **117**, 140-163 (1979).
57. Cunchillos, J.D. & De Andres, I. Participation of the cerebellum in the regulation of the sleep-wakefulness cycle. Results in cerebellectomized cats. *Electroencephalogr Clin Neurophysiol* **53**, 549-558 (1982).
58. Boehme, N.A., *et al.* Axonopathy precedes cell death in ocular damage mediated by blast exposure. *Sci Rep* **11**, 11774 (2021).

59. Perez-Garcia, G., *et al.* PTSD-Related Behavioral Traits in a Rat Model of Blast-Induced mTBI Are Reversed by the mGluR2/3 Receptor Antagonist BCI-838. *eNeuro* **5**(2018).
60. Corrigan, F., *et al.* NK1 antagonists attenuate tau phosphorylation after blast and repeated concussive injury. *Sci Rep* **11**, 8861 (2021).
61. Petrie, E.C., *et al.* Neuroimaging, behavioral, and psychological sequelae of repetitive combined blast/impact mild traumatic brain injury in Iraq and Afghanistan war veterans. *J Neurotrauma* **31**, 425-436 (2014).
62. Goldstein, L.E., *et al.* Chronic traumatic encephalopathy in blast-exposed military veterans and a blast neurotrauma mouse model. *Sci Transl Med* **4**, 134ra160 (2012).
63. Cernak, I., *et al.* The pathobiology of blast injuries and blast-induced neurotrauma as identified using a new experimental model of injury in mice. *Neurobiol Dis* **41**, 538-551 (2011).
64. Logsdon, A.F., *et al.* Nitric oxide synthase mediates cerebellar dysfunction in mice exposed to repetitive blast-induced mild traumatic brain injury. *Sci Rep* **10**, 9420 (2020).
65. Yaghouby, F., Donohue, K.D., O'Hara, B.F. & Sunderam, S. Noninvasive dissection of mouse sleep using a piezoelectric motion sensor. *J Neurosci Methods* **259**, 90-100 (2016).
66. Mang, G.M., *et al.* Evaluation of a piezoelectric system as an alternative to electroencephalogram/ electromyogram recordings in mouse sleep studies. *Sleep* **37**, 1383-1392 (2014).
67. Giesen, C., *et al.* Highly multiplexed imaging of tumor tissues with subcellular resolution by mass cytometry. *Nat Methods* **11**, 417-422 (2014).
68. Lein, E.S., *et al.* Genome-wide atlas of gene expression in the adult mouse brain. *Nature* **445**, 168-176 (2007).
69. Schapiro, D., *et al.* histoCAT: analysis of cell phenotypes and interactions in multiplex image cytometry data. *Nat Methods* **14**, 873-876 (2017).
70. Imai, K., Tingley, D. & Yamamoto, T. Experimental identification of causal mechanisms: Technical report Department of Politics, Princeton University (2009).
71. Imai, K., Keele, L., Tingley, D. & Yamamoto, T. Causal mediation analysis using R. In *Advances in Social Science Research Using R*, Vol. 196, ed. Vinod, H. (Springer, New York, NY, 2010).
72. Bittar, A., *et al.* Neurotoxic tau oligomers after single versus repetitive mild traumatic brain injury. *Brain Commun* **1**, fcz004 (2019).